



OLLSKOIL NA GAILLIMHE  
UNIVERSITY OF GALWAY

---

---

**Using the Wide-field Infrared Survey Explorer  
(WISE) Satellite Data to Identify Exceptional Planet  
Forming Disks**

*Introduction Report*

---

---

Name: Niamh O Toole

Student ID: 20343851

Supervisor: Dr. Christian Ginski

# Contents

<b>1 Abstract</b>	<b>1</b>
<b>2 Introduction</b>	<b>1</b>
<b>3 Star Formation</b>	<b>2</b>
<b>4 Protoplanetary Disks</b>	<b>4</b>
4.1 Planet Formation in Protoplanetary Disks . . . . .	5
4.2 Disk Substructures . . . . .	7
4.3 Cavities . . . . .	7
4.4 Spiral Arms . . . . .	9
4.5 Rings . . . . .	10
4.6 Bright Disks in Scattered Light Images . . . . .	11
<b>5 Spectral Energy Distributions</b>	<b>12</b>
<b>6 WISE Satellite Mission</b>	<b>15</b>
<b>7 High Contrast and High Resolution Images</b>	<b>17</b>
7.1 Very Large Telescope and SPHERE Adaptive Optics (AO) System . . . . .	17
7.2 Post-Processing Techniques to Remove Stellar Light from Images . . . . .	18
7.3 High Contrast Image Example . . . . .	19
<b>8 Project Outline</b>	<b>21</b>
<b>9 Methodology</b>	<b>22</b>
9.1 Sample . . . . .	22
9.2 Predicting Brightness of Disks from WISE Flux Excesses . . . . .	22

9.2.1	WISE Slopes	22
9.2.2	Converting WISE Magnitudes to Flux Densities	23
9.3	Directly Measuring Brightness of Disks from High Contrast Images	25
9.3.1	High Contrast Observations	25
9.3.2	Aperture Placement	25
9.3.3	Background Noise Calculation	26
9.3.4	Calculation of Disk Brightness in Scattered Light	27
<b>10</b>	<b>Results and Discussion</b>	<b>28</b>
10.1	Classification of Sample into Bright or Faint Disks	28
10.2	Brightness Profiles	30
10.3	Comparison of Disk Brightness with WISE Slopes.	30
10.4	Disk Dust Mass	33
10.5	Finding a New Sample of Disks to Image	36
10.5.1	Constraints for Finding New Sample of Disks	36
<b>11</b>	<b>Conclusions</b>	<b>39</b>
<b>12</b>	<b>Future Work</b>	<b>41</b>
12.1	Plagiarism Declaration	43
12.2	Data References	43
<b>13</b>	<b>Appendices</b>	<b>48</b>
13.1	Appendix A. Python Code Written in this Work	48
13.2	Necessary Libraries	48
13.3	Query Disk Sample WISE Magnitudes	49
13.4	Calculate the WISE Slopes using the WISE Magnitudes	50

13.5 Measuring the Brightness Ratio of the Disks in the Sample from the High-Contrast Images . . . . .	52
13.6 Plotting the WISE Slopes against the Disk Brightness Ratios . . . . .	58
13.7 Finding a New Sample of Disks that are Predicted to be Bright . . . . .	60
13.8 New Sample of Disks Predicted to be Bright . . . . .	63

## 1 Abstract

*Context.* Circumstellar, protoplanetary disks are disks of gas and solids around young stars and are the birth places for planets. Disk structures are imprints for hidden planets in disks, these are variations in the spatial distribution of the disk material. These structures should be studied to extend our understanding of the planet forming process. High-contrast, high-resolution images of disks are required for this analysis. Disks must be bright, i.e., the whole disk must be illuminated by stellar light, for the structure to appear in images. Advancements in ground based imaging instrumentation over the past decade has improved the ability to observe these planet forming environments. Imaging of the disks in near-infrared scattered light uses the fact that small dust particles in the disks scatter light from the central star which can be detected. Not all disks are bright in scattered light due to their structure. Those which are allow the study of their structure.

*Aims.* The aim of the project is to predict disks which should be bright in scattered light and would be ideal targets for future observations of disks to be imaged in high-contrast by the Very Large Telescope (VLT).

*Objectives.* To predict the brightness of disks, photometric data from the WISE Satellite mission is used to plot Spectral Energy Distributions (SEDs). SEDs show the flux excess in the infrared region from disks as compared to the flux from the star. SEDs are a frequently used technique for determining the structure of protoplanetary disks. By doing this, the brightness of the disk can be predicted based on its structure. To confirm the accuracy of these predictions, the brightness of disks will be directly measured from high-contrast images and the predictions can be refined. Once this is achieved, predictions for the brightness of disks which have not previously been observed will be made and this will suggest a new sample of disks which should be imaged in the future.

## 2 Introduction

Planets form in circumstellar disks which are disks of gas and solids that orbit a central young star. These disks develop around stars as they form. After a few million years the material in the disk is used up and a solar system is formed around the star, much like our Sun and planets. How exactly these planets are formed is still a topic that is much debated today. The hallmarks of the planet-forming process are traced by the disk structures. The disks can feature structures such as rings, gaps, spiral arms and cavities, which can be used to predict hidden

planets in the disk. These structures can be studied in high resolution images of disks. In order for the structure to be visible in the image the disk must be bright, i.e., the stellar light must be able to illuminate the majority of the disks surface so that light is scattered from all regions of the disk. This scattered light is detected by telescopes. To further develop our theories on planet formation, we need to observe more protoplanetary disks in high-resolution images and analyse their structure. By predicting which disks are bright ahead of making observations, we optimize our chances of imaging disks which will display this structure and be useful to further our understanding of how our own planet and planets outside of our Solar System form.

### 3 Star Formation

The presence of luminous, hot stars throughout different galaxies is clear evidence that stars are regularly forming. Their mass and large luminosity indicate that they have lived for a short period of time. This means there are plenty of stars whose disks can be observed with the aim of identifying planets which are forming or have formed.

Stars are born in regions of gas and dust called molecular clouds. These are composed of atoms, molecules, and dust, with the dust grains being larger bodies of matter up to a few millimetres in size. The clouds have a complex mixture of hydrogen, oxygen, carbon, nitrogen, and sulfur compounds and the dust grains possibly contain various silicates, magnetite, and carbon compounds, and water ice, [Prinn \[1993\]](#). Hydrogen and helium are typically the most abundant gases found in molecular clouds, with the other gaseous compounds being present in much smaller amounts. Molecular clouds typically have temperatures as low as 10K which means they emit radiation at very long wavelengths which are hard to detect. The dust grains emit thermal radiation, which can be observed at sub-millimetre (mm) wavelengths, and absorb background light from stars, which can be observed at near-infrared (IR) wavelengths. These observation techniques give a good picture of the structure of molecular clouds within the Milky Way but cannot be used for extra-galactic clouds as they are too far away and blocked by nearer stars, [Krumholz et al. \[2011\]](#).

The first stage of star formation is induced by the turbulent motion within the cloud, this motion causes the gas and dust to move around over time, [Krumholz et al. \[2011\]](#). This non-viscous motion allows particles to collide within the cloud and clump together. In this way, material can build up in a region with a small radius and large density. The internal pressure in this region must balance with the external force of gravity at all points in the cloud. As the mass continues to increase, a maximum pressure is approached and the cloud becomes progressively

more unstable, [Krumholz et al. \[2011\]](#). This results in a maximum mass that the cloud can reach, above this mass the internal pressure is not strong enough to balance the gravitational force and the cloud collapses due to its own self-gravity. This mass is called the Jeans mass.

By assuming a star is a blackbody, a state of local thermodynamic equilibrium (LTE) can be assumed, [Ellis \[2011\]](#). This simplification allows the structure of the star to be given by simplified equations. The instability requirement for collapse is given by the hydrostatic equilibrium expression, the simplified formula is:

$$\frac{dP}{dr} = -\frac{GM(R)}{R^2}\rho \quad (1)$$

where  $P$  is the pressure,  $G$  is the gravitational constant,  $R$  is the radius and  $\rho$  is the density. The negative sign on the right-hand side indicates that the pressure decreases outward in the system. This equation leads to the Jeans mass, an upper limit for the mass that can sustain hydrostatic equilibrium, [Ellis \[2011\]](#),

$$M_J \approx 10^5 \frac{T^{\frac{3}{2}}}{\sqrt{n}} M_{\odot} \quad (2)$$

where  $T$  is the temperature,  $n$  is the number of gas particles per  $m^3$  and  $M_{\odot}$  is the mass of the sun. When the mass of the cloud exceeds this mass, the cloud will fragment and collapse.

A pre-stellar core is created when the cloud collapses and this core starts to accrete gas surrounding it. Gas and solid particles are attracted by the gravitational pull of the stellar core and the system rotates. To conserve the angular momentum of the star, the rotating gas and dust forms a disk around the core. This is the circumstellar disk where planets are formed. The gas and dust are suspended in the disk due to their angular momentum, however some gas fragments will have lower angular momentum causing them to fall in on the pre-stellar core. Other fragments will have higher angular momentum and will move away from the star, [Mariotti and Alloin \[1999\]](#). The gas accretion by the core causes the production of anisotropic outflows and highly collimated jets, [Mundt and Ray \[1994\]](#). Such outflows are formed from the interaction of the accreting gas with the stellar magnetic fields and surrounding fields.

As the mass continues to grow from accretion of the surrounding material, the gravitational energy released is turned into thermal energy. The opacity of the gas increases as the density and temperature increase and once the gas becomes opaque to its own radiation, it is defined as a young star. When hydrostatic equilibrium is reached again, the embryo becomes a protostar, [Ellis \[2011\]](#). The protostar continues to accrete material and build up in mass, and its temperature continues to increase. Once a high enough temperature is reached, nuclear fusion is ignited

in the core and the star is defined as a main-sequence star, like our Sun. In this phase, the star is fusing hydrogen into helium and this is the longest stage of a stars life.

Young stars can be divided into different classes which represent their evolutionary stages. T Tauri stars are pre-main sequence stars with optically thick circumstellar disks, observable in near-IR region. They have mass of roughly our own sun or lower. There is a decrease in the accretion of matter by the core and it is expected this is the phase where planet formation begins. Higher mass young stars are called Herbig stars, they have masses from approximately  $1.5M_{odot}$  to  $2.5M_{odot}$ . These stars are the class of stars that should be observed to learn more about planet formation.

## 4 Protoplanetary Disks

Disks are expected to display a flaring surface due to the heating of dust grains by the stellar radiation. T Tauri stars have optically thick protoplanetary disks, which have an optically thin upper-layer of dust grains that become super-heated by the radiation as they are directly exposed to it, [Chiang and Goldreich \[1997\]](#). The heating of the disk from the stellar radiation causes the disk to flare, as seen in figure 1. A midplane can be defined at the centre of the disk and surface height  $H$ , is the height from this midplane to the surface of the disk, [Mariotti and Alloin \[1999\]](#). This increases further out in the disk due to the flared structure. The heated dust grains emit approximately half the stellar energy they absorb directly into space and the other half is emitted inwards and heats the disk interior, [Chiang and Goldreich \[1997\]](#). In this way, disks are heated from the outside leading to the temperature decreasing from the surface to the disk midplane. Therefore, gas and dust features can be seen in emission, [Garcia \[2011\]](#).

Photons from the star are scattered by the upper surface layer of disks. This allows the surface shape of the disk to be clearly seen and measured from scattered-light images, [Benisty et al. \[2023\]](#). Substructures, such as rings, spiral arms and cavities are frequently seen in disks and are the main evidence for planet formation.

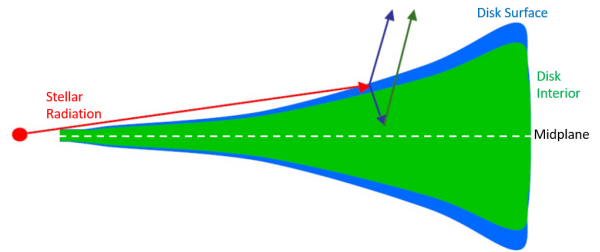


**Figure 1:** Schematic of an optically thick protoplanetary disk. The blue region is the optically thin disk surface and the green region is the disk interior. The midplane of the disk is shown. Image credit: [Woitke \[2015\]](#) (modified)

## 4.1 Planet Formation in Protoplanetary Disks

T Tauri and Herbig stars are the stellar types this project will focus on as they are in the evolutionary stage where planet formation is expected to occur. In this stage there is a reduction in the accretion of matter by the star and the gas and dust remains in motion in the circumstellar disk, the motion of the material leads to planet formation.

The initial stages of planet formation involve the coagulation of dust grains, followed by gas accretion in the case of giant planets, [Mariotti and Alloin \[1999\]](#). They grow from the initial sub-micron sizes to the hundred kilometre (km) sizes of planetesimals ([Brandner \[2006\]](#)) through collisions, and sticking and accumulation of particles, [Weidenschilling and Cuzzi \[1993\]](#). The evolution of the dust within the disk is thought to depend on its position within the disk, radially and vertically. The interaction between the gas and dust leads to dust growth and this interaction determines the relative velocity and the distribution of dust grains in the disk, which are both critical for grain growth, [Brandner \[2006\]](#) The relative velocities between grains determine the collision rates and outcomes of collisions; sticking and growth of particles occurs when relative velocities are low enough, ([Brandner \[2006\]](#), [Poppe et al. \[2000\]](#)). If velocities are too high, collisions can lead to destruction of grains and thus, the production of smaller grains. Dust and gas are coupled in the disk with smaller grains being almost perfectly coupled to the gas particles as opposed to larger grains. This allows small particles, approximately  $\lesssim$  micrometre( $\mu m$ )-sized, to mix well with the gas except at the disk surface and they become easily mixed in the disk by turbulence. They also have low velocities, therefore, the smallest grains in the disk will start to aggregate first, [Brandner \[2006\]](#). Van der Waals bonds will form between these small particles to allow them to stick together. Electrostatic forces also act between the particles, [Weidenschilling and Cuzzi \[1993\]](#).

As dust grains collide and grow into larger aggregates, they tend to settle towards the midplane of the disk; larger grains will settle faster and in this process will sweep up smaller grains. The dust will then dominate the midplane layer and the gas will be dragged along with the dust. This has the effect of reducing the relative velocities between different sized particles. This leads to the growth of particles to metre sizes and gradually to the formation of km-sized planetesimals. Particles larger than approximately 1 km will fully decouple from the gas, and planetesimals grow by runaway accretion, where the largest bodies grow fastest and produce objects of  $\sim 100$  km in size. Once these bodies become large enough, the growth process switches to gravitational attraction of planetesimals to each other. A terrestrial planet, similar to Mars, is formed once all the planetesimals within gravitational reach are combined. When

the orbits of these bodies cross, they can collide to create larger terrestrial planets like Earth. The timescale for this process is in the range of 10-100 million years (Myr), [Brandner \[2006\]](#).

Gas giant planets can form through core accretion. As the planetesimals increase in mass, a critical value of 10 Earth Masses is reached, beyond which the body starts to attract gas onto its surface. This is expected to happen through gas accretion onto a solid core. The process starts off the same as terrestrial planet formation with dust coagulation up to km-sized planetesimals surrounded by a gaseous envelope, [Bodenheimer et al. \[2000\]](#). Assuming the size of the planetesimals remain in the km range, giant-planet cores are estimated to form on a 1 Myr timescale which is fast enough to accrete a massive atmosphere of gas from the disk. The accretion of gas steadily increases until it exceeds the rate at which solids are being accreted. The planetesimal is now a protoplanet and the gas accretes at a constant rate until runaway gas accretion occurs and the protoplanet begins to rapidly increase in mass. The production of a gap in the disk stops the accretion, the protoplanet contracts and cools, and a gas giant planet is left, [Brandner \[2006\]](#).

The formation of gas giants by core accretion can take up to 100 Myr, which is longer than the typical lifetimes of protoplanetary disks. The lifetime of disks can be examined by looking at the fraction of stars with near-infrared excess as a function of stellar age. Protoplanetary disks typically dissipate after about 10 Myr for low mass stars, whereas disks around higher mass stars dissipate after as little as 1 Myr. The frequency of accretion disks steadily decreases from less than 1 to approximately 10 Myr, [Williams and Cieza \[2011\]](#). Therefore, gas giant planet formation would be rare. However, the frequent detection of such planets indicates they are not rare which suggests there must be a separate method of formation for these planets. Giant gaseous protoplanets (GGPPs) can form rapidly in cool regions of disks through gravitational instability. This instability depends on self-gravity overwhelming the thermal pressure in the disk. The process of gravitational instability involves the disk breaking up into clumps of gas and dust through its own self-gravity, [Boss \[1997\]](#). These clumps then contract and collapse to form giant planets, [Bodenheimer et al. \[1980\]](#). Initial research in the area of gravitational instability suggested that the formation of spiral waves in disks could lead to them being marginally unstable but GGPPs could only form in strongly unstable disks, [Laughlin and Bodenheimer \[1994\]](#), [Cassen et al. \[1981\]](#). It was also suggested that GGPP formation required the instability to occur at a fixed temperature at a given radius, [Cassen et al. \[1981\]](#). A parameter called the Toomre parameter, denoted by  $Q$ , is assigned to disks to indicate their stability. If  $Q$  is less than 1; GGPPs can form through gravitational instability. For marginally unstable disks the GGPP instability is expected to occur if a condition exists to cause  $Q$  to fall below 1. One

such cause is the clumpy accretion of molecular cloud gas by the disk which increases the disk's surface mass density allowing  $Q$  to drop below 1, triggering the instability required. If rock and ice materials are present in the disk in the form of dust grains, they can settle to the center of the GGPP and form an ice and rock core. As the GGPP evolves it will slowly contract until its central temperature becomes high enough to vaporize rocky dust grains and for water to become soluble in hydrogen. As this happens the gas pressure gradient prevents the protoplanets gas from collapse, and the dust grains coagulate and settle towards the centre of the GGPP. This happens in a similar way to the coagulation and settlement of dust grains to the midplane of the disk. Cm-sized grains coagulate and sediment to the center of the GGPP and a substantial rock and ice core forms in the center. The GGPP eventually heats up, dissociates its molecular hydrogen, and collapses to planetary densities, [Boss \[1997\]](#).

Larger grains in the protoplanetary disks settle towards the midplane, as discussed. Therefore, mm- to cm-sized grains will be found in the midplane. The smallest grains, as small as  $0.1\mu m$ , will be closest to the surface layer of the disk which is directly heated by the stellar radiation. It is expected that planet formation occurs mainly in the midplane of disks and this suggests why so few planets have been detected in circumstellar disks; they may be embedded in these optically thick disks and cannot be seen. This is why we rely on the structure of the disks to identify hidden planets that have formed. Substructures in disks can be seen in scattered light images at optical and near-IR wavelengths, the stellar light is scattered by the small grains in the surface of the disk. Scattered light images trace the  $\mu m$ -sized grains in the disk which are coupled well to the disk gas. Therefore, we can trace properties of the gas by looking at the light scattered by the small grains in near-IR images.

## 4.2 Disk Substructures

## 4.3 Cavities

Substructures can be created through planet-disk interactions due to how planets create a path as they deplete the disk of its material. Disk structures can be traced in multiple wavelengths and each wavelength highlights different constituents of the disk. Large particles will emit light at longer wavelengths, therefore, mm-observations will trace the larger grains which are closer to the disk mid-plane. Long wavelengths correspond to thermal emission from the disk at cold temperatures. Whereas, the scattered light in the near-IR observations trace the  $\mu m$ -sized grains at the disk surface, and thus the gas as these small grains are well coupled to it.

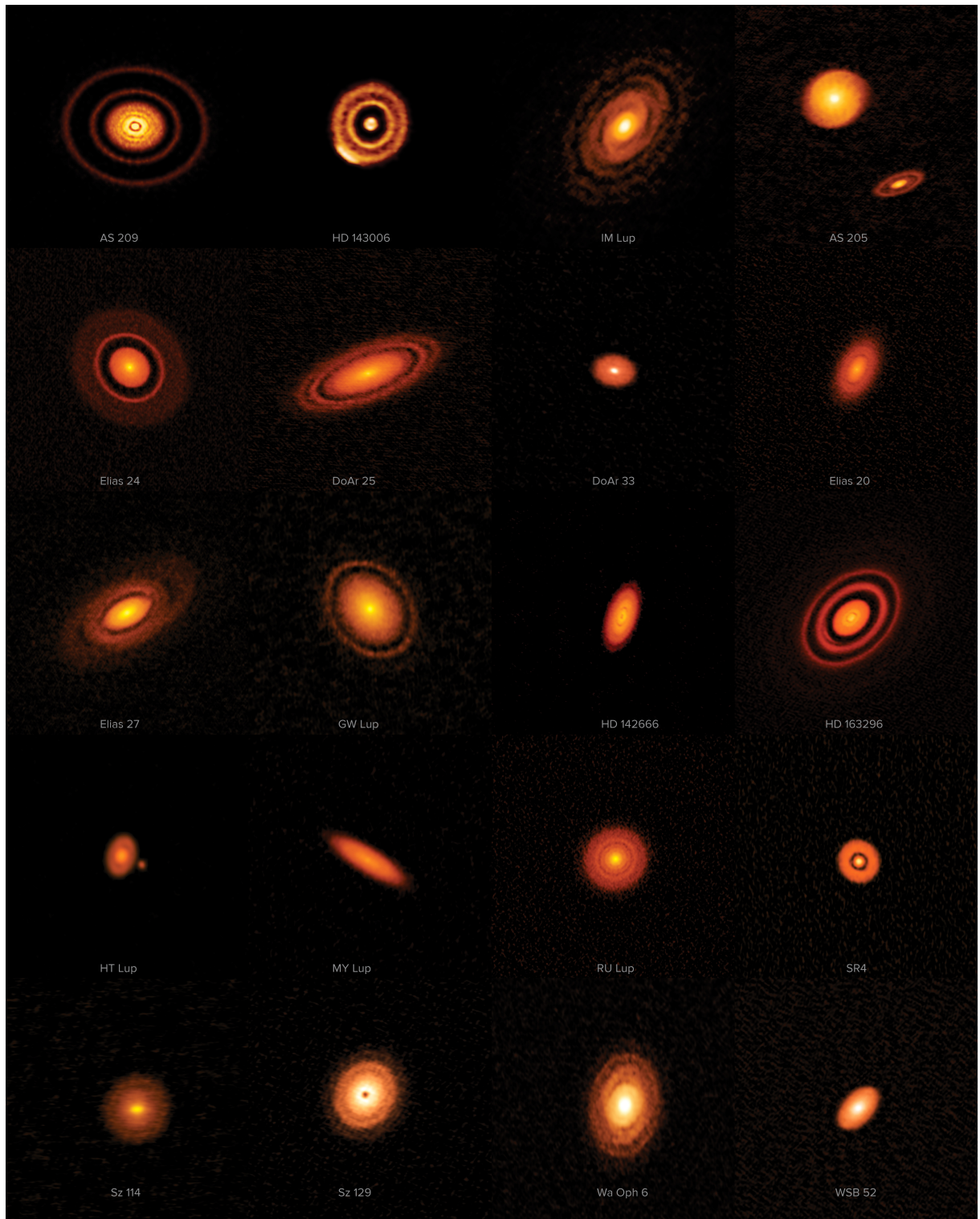


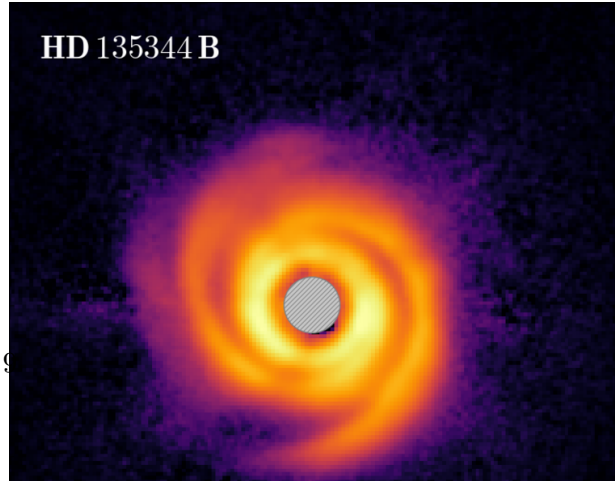
**Figure 2:** 20 protoplanetary disks captured by ALMA (Atacama Large Millimetre Array) Radio Telescope. Image displays the diversity in the size and structure of disks. The name of each star at the centre of the disks is at the bottom of each image. Credit:ALMA (ESO/NAOJ/NRAO), S. Andrews et al.; NRAO/AUI/NSF, S. Dagnello

Large regions close to the star, typically 10s of AU in size, which are significantly depleted of  $\mu\text{m}$ -sized dust grains are defined as cavities. [Pinilla et al. \[2018\]](#) suggested that the formation of such cavities is possibly explained by a giant planet present in the disk clearing up material, internal photoevaporation, or regions of low disk ionization. If cavities are formed due to giant planets depleting the disk of its material, this suggests a possible relation between the stellar and disk mass and the cavity size. Regions of the disk with low ionization are known as dead zones. These zones can create cavities when a pressure bump is formed at the edge of the region. In this bump, particles can grow and accumulate which causes a dust-cavity depleted of small grains. Photoevaporation involves radiation from the star heating the disk material sufficiently that it becomes unbound from the star and flows from the disk as a wind ([Alexander and Armitage \[2007\]](#)), potentially leaving behind a cavity. Regardless of the way in which the cavity forms, it is expected that mm-sized particles will be trapped near or further out of the edge of the cavity, [Pinilla et al. \[2018\]](#). Cavities often only extend to around 10 AU, which is too small to be spatially resolved by our telescopes for a star at a distance of approximately 150 pc, the distance of nearby star forming regions. They can be imaged by radio telescopes by detecting the emission from mm-sized dust grains. This is also allowed by the fact that the cavities are depleted of the micron-sized grains and the larger grains are trapped at the cavity edge. This allows the cavities to be larger in radius in long wavelength observations and smaller in near-IR scattered light images.

Cavities directly influence the brightness of disks by affecting how much of the disk is illuminated by stellar light. Disks with large cavities near their centre tend to be the brightest disks as the light from the star can reach the outer regions of the disk as it will not be blocked by any dust grains that otherwise would be present. The presence of a dust cavity in the inner disk can be identified by a lack of near-IR emission emitted by the disk. This is seen on a Spectral Energy Distribution (SED) which displays the energy emitted by a disk at different wavelengths.

#### 4.4 Spiral Arms

Planet-disk interactions can create paths of depleted material that travel through the disk as a spiral wave, [Benisty et al. \[2023\]](#). Spiral arms are caused by local perturbations of the disk surface density and/or the scale height, [Stolker et al. \[2016\]](#). The arms are defined by



their pitch angle which is the angle the spiral makes with a circle around the star and they can span tens to hundreds of AU. The pitch angle becomes larger for more massive planets. Some disks feature two nearly symmetric arms, while others show multiple symmetric arms, [Benisty et al. \[2023\]](#). It has been shown that one-armed spirals can be produced due to density waves being excited by low-mass protoplanets that are embedded in the disk at certain resonances, [Goldreich and Tremaine \[1979\]](#). Figure 3 is a scattered light image of the disk around HD135344B. The image was taken using the IRDIS<sup>1</sup> near-IR subsystem of the extreme adaptive optics imager SPHERE of the Very Large Telescope<sup>2</sup>. The image displays the spiral arms, there is also a 25 AU cavity present in the disk, [Stolker et al. \[2016\]](#). The cavity is not seen in the image as it is too small to be resolved in the image, it would be visible in mm-continuum emission.

#### 4.5 Rings

In certain regions of disks, radial gradients in temperature and density can cause the gas to form a solid, these regions are called condensation fronts. The change in chemistry and opacity in these regions can cause a pressure gradient that can allow dust particles to collect. Instability can arise through the vertical settling of dust in the disks which creates vertices where the dust can collect, this causes the ring-shaped features seen in some disks. The production of gaps within disks and their geometry depend on the thermal and viscous properties of that region of the disk. For ex-

<sup>1</sup>Infra-Red Dual Imaging and Spectrograph (IRDIS)

<sup>2</sup>Spectro-Polarimetric High contrast imager for Exoplanets REsearch (SPHERE), will be discussed along with the VLT in section 7.1

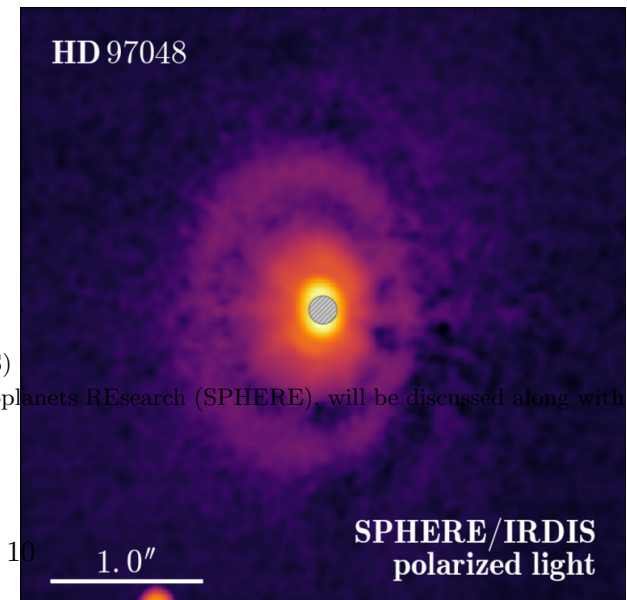


*Figure 4:* Scattered light image of the disk around

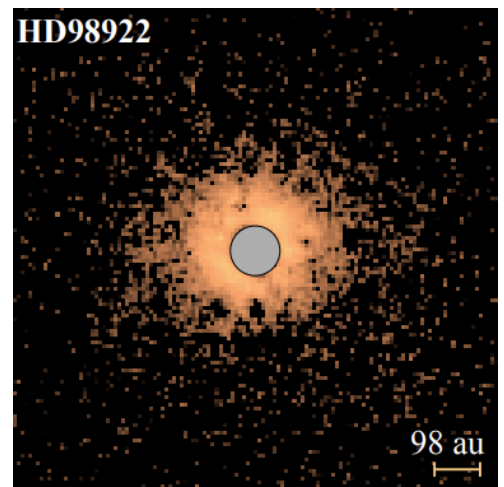
ample. the viscosity of the disk determines the depth and width of the gap. The gap is formed by a transfer of angular momentum from the planet to the gas. Density maxima inside and outside gaps in the disk can arise depending on the disk viscosity and temperature. Dust can also collect in these regions and lead to ring-like features, [Benisty et al. \[2023\]](#).

Figure 4 is an image of the disk around HD97048. The scattered light image reveals HD97048 has a bright disk that features four ring-like structures (only 2 of these rings are visible in this image) and corresponding gaps, [Ginski et al. \[2016\]](#). The star is known to have a large circumstellar disk possibly larger than 600 AU, [Doering et al. \[2007\]](#). A scale bar of 1" appears in the image, this corresponds to approximately 184 AU for an assumed distance of  $\sim$ 184 parsecs<sup>3</sup>. The disk features a cavity out to approximately 43 AU ([van der Plas et al. \[2016\]](#)), which allows the rest of the disk to be illuminated by the stellar light, revealing its structure in the image. The cavity is not visible in this image, it would be visible in mm-continuum emission as with the cavity for the disk in figure 3.

#### 4.6 Bright Disks in Scattered Light Images

Scattered light images can be used to study the sub-structures of disks that possibly point to planets that are forming in the disk. The amount of scattered light observed from a circumstellar disk depends on many factors. How much light reaches the observer depends largely on the number of photons that reach the disk surface and the geometry of the disk. This depends on the stellar luminosity and the possible presence of a cavity in the inner region of the disk, [Benisty et al. \[2023\]](#). If there is no cavity present, the dust grains in the centre of the disk shadow the outer regions. The

<sup>3</sup>1 parsec is  $\approx 3 \times 10^{13}$  km. The distance in parsecs is found from the parallax measurement for the star given in the SIMBAD database. Dividing the parallax by 1000 gives the distance in parsecs.



**Figure 5:** Scattered light image of the faint disk around HD98922. The name of the star is given in the top left corner and a scale bar is in the bottom right. The grey circle indicates the region obscured by a coronagraph. Image credit: [Garufi et al. \[2016\]](#).

illumination of the disk by stellar radiation scales as a function of distance from the star, [Benisty et al. \[2023\]](#). As the distance from the star increases, the decrease in illumination is proportional to  $1/(4\pi r^2)$ , [Benisty et al. \[2023\]](#). Dust grains which are further away from the star are illuminated by less radiation per unit area than grains closer to the star and will scatter less photons. Therefore, the brightness of the disk decreases towards its outer regions. Many other factors influence the observed brightness of the disk such as the dust albedo, which is the dust grains efficiency in scattering photons at specific wavelengths, [Benisty et al. \[2023\]](#).

Faint disks arise due to the geometry and structure of the disk. Self-shadowing is a common cause of faint disks, [Benisty et al. \[2023\]](#). This occurs when there is a lot of dust grains in the centre of the disk near the star. The inner disk material is directly exposed to stellar radiation and becomes hot and puffed up, blocking the stellar light from reaching the outer disk and causing a shadow across the disk, [Garufi et al. \[2022\]](#). Shadows can also form due to misalignment of the inner disk, [Benisty et al. \[2023\]](#). Faint disks can also be due to disks which have very little to no dust grains and particles in them, therefore very little light is scattered by the disk. Some disks are too small to resolve with high resolution with current telescopes. These disks may be bright and may have planets forming in them but they are not ideal to observe as current telescopes cannot resolve their detail. An image of the faint disk around HD98922 is shown in Figure 5. The image is a near-IR observation obtained with IRDIS and SPHERE. The structure of the disk is not visible in the image which is what is required to be observed in order to deduce information about possible forming planets in the disk. The sub-structures of disks that can be studied to further our understanding of planet formation are typically not visible in scattered light images of faint disks. However, these disks can be looked at to learn more about disk evolution and dust grain properties. It is more ideal to image bright disks for planet formation studies. It is important to predict the brightness of disks ahead of making observations to optimize valuable observation time and increase the chance of obtaining images where the sub-structure is visible.

## 5 Spectral Energy Distributions

All celestial bodies emit electromagnetic radiation that depends on their temperature. The wavelength of energy emitted by a body is directly related to the temperature, objects with

higher temperatures will emit energy of a shorter wavelength compared to colder objects. This thermal emission from the system can be plotted on a Spectral Energy Distribution (SED). The diagram in Figure 6 shows a schematic example of a simplified SED for an optically thick disk. The graph shows the flux from an object as a function of different wavelengths while also showing the temperature relationship. Flux is the amount of energy from a luminous object that hits a surface over a certain time period, this can be measured from Earth for any object and plotted on a SED. The flux is measured in Janskys, which is  $Wm^{-2}Hz^{-1}$ , and the wavelength is measured in micrometres. The structure of young stellar objects and their disks can be inferred from SEDs by analysing the amount of energy emitted at different wavelengths, this is the most frequently used technique for discovering new disks and characterising their structure, [Woitke \[2015\]](#). SEDs can indicate the presence of a cavity within a disk as there will be a decrease in the energy due to the depletion of dust grains in the inner region of the disk, this is demonstrated in Figure 6.

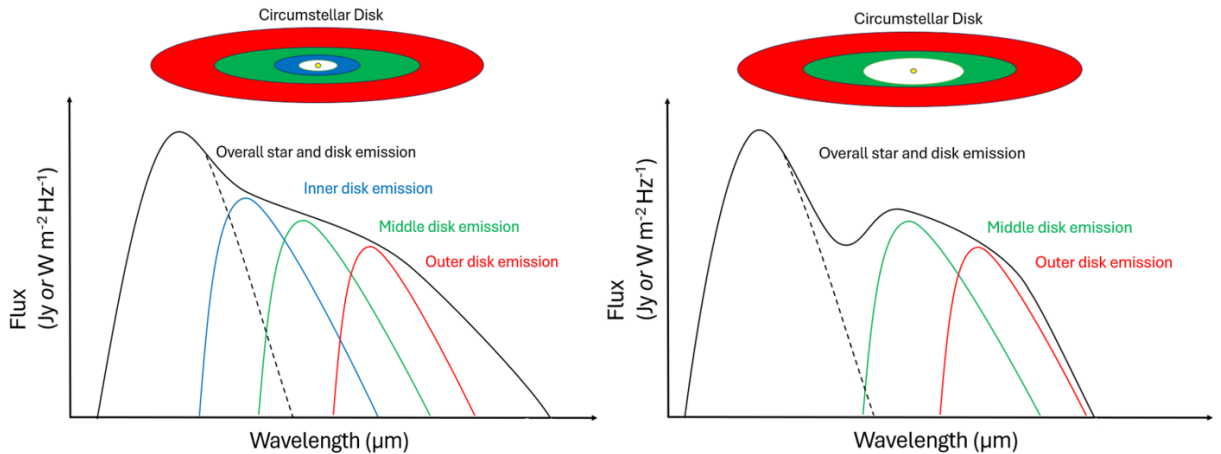


**Figure 6:** Schematic diagram of an SED for an optically thick disk with and without a large inner cavity. The plots show the flux detected from the star and the disk as a function of wavelength. The flux is measured in Janskys where  $1Jy = 1Wm^{-2}Hz^{-1}$  and the wavelength is measured in micrometres. The black line corresponds to the overall star and disk emission, the black dashed line indicates the blackbody curve for the star. The blue line indicates the inner disk emission, this is in the near-IR region, typically centred around  $10\mu m$ . The green line shows the emission from the middle of the disk and the red line shows the emission from the outer region of the disk.

Circumstellar disks are detected mainly through flux excesses, the infrared to millimetre flux excess compared to the flux from stars without disks, [Woitke \[2015\]](#). The young star and its disk is observed in the near- and far-IR wavelength regions and the sub-mm region. The SED of a star resembles a blackbody curve, given by the Planck function, [Ellis \[2011\]](#):

$$B_\nu(T) = \frac{2h\nu^3}{c^2} \frac{1}{e^{\frac{h\nu}{kT}} - 1} \quad (3)$$

For a young star with an accretion disk the distribution is a blackbody curve with energy peaks at longer wavelengths. The star is the hottest object in the system so the energy emitted by the star will dominate the shortest wavelength regions in the distribution. The inner disk material will emit energy at wavelengths just above that of the star as the material is heated to high temperatures by the star. The material in the outer regions of the disk emits energy of longer wavelengths as the dust grains here are cold as they are far from the stellar light.

Figure 7. shows an example of an SED for the Herbig star HD163296 (Woitke [2015], Tilling et al. [2012]). At wavelengths below  $1\mu\text{m}$ , the stellar radiation dominates, this is usually below  $2\mu\text{m}$  for T Tauri stars. At these wavelengths, the disk is too cold to contribute any thermal emission to the SED (Woitke [2015]), therefore analysing this region does not convey any information about the disk. The red line which follows the peak in this region and rapidly decreases outside this region shows the blackbody curve for the star without its disk. The flux from the star drops off in the near-IR region and falls to zero around  $100\mu\text{m}$  in the far-IR region. There is still energy detected from the system at these longer infrared wavelengths, this flux corresponds to the disk. The near-IR region is from  $1\mu\text{m} - 5\mu\text{m}$ , this strong excess is from the hottest grains in the disk which lie in the inner region of the disk, Woitke [2015]. These grains will be closest to the star and will be illuminated by a stronger flux than dust grains further out in the disk. This leads to them having a high temperature and they emit energy at these near-IR wavelengths. The next region from  $5\mu\text{m} - 30\mu\text{m}$  is known as the silicate emission region. This region shows strong silicate dust emission features at  $10\mu\text{m}$  and  $20\mu\text{m}$  in particular, Woitke [2015]. Photons detected at these wavelengths are mostly emitted from grains in the upper regions of the inner disk, the energy emitted in this region can be used to deduce information about the composition and size of the dust grains in these regions. The last two regions at wavelengths longer than  $30\mu\text{m}$  display the energy detected from the outer section of the

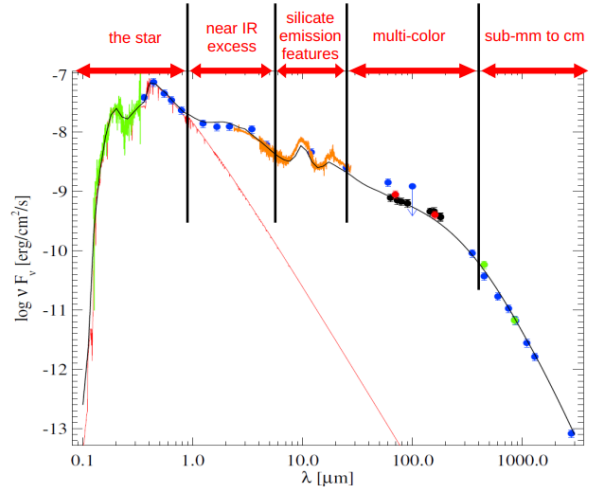


**Figure 7:** The SED of the star HD 163296. The blue, red, black, and green circles with errorbars are photometric data points obtained from different instruments. The black line corresponds to the disk thermal emission and the red line indicates the blackbody curve for the star. The SED is sub-divided into 5 regions which indicate different regions of the disk and wavelengths of the emission. Image credit: Tilling et al. [2012] reproduced and modified by Woitke [2015].

disk, [Woitke \[2015\]](#). The dust grains here are far from the stellar core and the flux from the star is spread over a larger area so the grains are much colder. Therefore the light scattered by these grains has a longer wavelength, in the far-IR region heading towards the sub-mm and cm regions.

SEDs can be used to predict the brightness of circumstellar disks through analysis of the near-infrared (NIR) flux excesses and the far-infrared (FIR) excesses. Disks which are bright typically have a large cavity in the inner regions of the disk, this can be indicated in SEDs by a dip in the flux in the NIR region as shown in figure 6. This dip is typically around  $10\mu\text{m}$ . A subsequent increase in the flux in the FIR region establishes that the stellar radiation is reaching the outer disk and there is a presence of dust grains here emitting energy at these longer wavelengths. Therefore, SEDs with low NIR excess and high FIR excess should indicate a disk with a cavity which is likely bright in scattered light.

In comparison, faint disks are indicated by SEDs with:

- (i) Low NIR excess and low FIR excess. SEDs which show this correspond to disks which have almost no dust grains in them. The absence of material means little to no energy is emitted across the whole disk.
- (ii) High NIR excess and high FIR excess, these excesses point to self-shadowed disks. Disks become self-shadowed when there is a lot of dust grains in the inner region of the disk near the star. The high NIR excess correlates to a lot of material in this area, at high temperatures that emit energy in the NIR region. The high FIR excess shows there is still an extended disk containing significant amounts of dust grains which emit energy at these wavelengths. However, the high NIR excess shows that this area of the disk will be shadowed and will not be visible in images.
- (iii) SEDs with high NIR excess and low FIR excess relate to disks which are small. The disks may be too small to resolve with high resolution with current telescopes. The low level of FIR excess points to this as almost all the energy emitted is in the shorter near-infrared range meaning most of the material is close to the star.

## 6 WISE Satellite Mission

The main aim of this project is to predict brightness of disks in order to compile a sample of disks which have not yet been observed that should be bright. The brightness of disks can be predicted by analysing the thermal emission from the system using SEDs. In this project, SEDs will be plotted for many disks using data collected by the WISE Satellite Mission.

The WISE Satellite was launched in 2009 with the aim of mapping the entire sky in four infrared bands centred at  $3.4\mu m$ ,  $4.6\mu m$ ,  $11.6\mu m$  and  $22.1\mu m$ . The Satellite has much higher sensitivity as compared to previous infrared survey missions, [Wright et al. \[2010\]](#). The InfraRed Astronomical Satellite (IRAS), [Neugebauer et al. \[1984\]](#), is a similar previous mission which was launched in 1983, this mission mapped the whole sky in four bands also and featured 62 detectors. WISE used a 40 cm telescope with arrays featuring a total of 4 million pixels. This allowed WISE to have a much higher sensitivity due to the increased number of detectors, its sensitivity was 100 times better than IRAS, [Wright et al. \[2010\]](#).

[Wright et al. \[2010\]](#) explains how WISE had many science goals, one such goal was to study star formation and the evolution of circumstellar disks. The satellite was capable of detecting the small IR excesses from disks by predicting the long-wavelength photospheric emission and by accurately measuring the total long-wavelength emission, this was enabled by the satellite's four colour photometry and sensitivity. The satellite aimed to find T Tauri stars with optically thick disks at substantial distances. The high sensitivity of WISE allowed this detection for stars out to 1 kpc distance, [Wright et al. \[2010\]](#).

The WISE satellite surveyed protoplanetary disks around thousands of stars. As micron-sized grains in disks combine into larger particles during planet formation, there is a reduction in grain surface area which makes the disks optically thin, and the infrared excess decreases significantly. The disk does not clear in a uniform way and this would be evident in the SEDs plotted from infrared excess measurements. By analysing these signals, WISE aimed to refine the timescales for disk clearing and solar system formation, [Wright et al. \[2010\]](#). It also provided a catalogue of data that could be used to plot SEDs to identify bright disks and provide future telescopes with hundreds of targets for high contrast and high resolution imaging. In this project, data will be retrieved from the WISE catalogue of data and used to plot multiple SEDs for different disks. These will be analysed to see if a dip appears in the near-IR region which would indicate the presence of a cavity, as discussed previously. Disks which feature this distinctive decrease in brightness will be predicted as bright disks. The WISE Satellite used broadband photometry to collect the data, this means the strong silicate emission peaks commonly seen in the near-IR region around  $10\mu m$  and  $20\mu m$  will not appear in the SEDs plotted from the satellites data. If these peaks appeared in the SEDs of disks with cavities, the dip in energy in the near-IR region would not be as clear and would affect the ability to form predictions.

## 7 High Contrast and High Resolution Images

Once the brightness of disks has been predicted through the SEDs plotted with the WISE data it is important to determine if this prediction is accurate. This is achieved through directly measuring brightness of disks which have been observed in high contrast images.

Protoplanetary disks are best observed through images with high contrast and high resolution. High contrast allows very faint objects to be observed next to something bright. This is required when observing circumstellar disks as scattered light from disks is significantly fainter compared to the light from the central star, [Garufi et al. \[2022\]](#). Very small objects can be observed through high resolution images. Many of the stars with protoplanetary disks that are observed are huge distances away and are therefore extremely small on the sky. Telescopes with large apertures are needed to observe objects this small with high resolution.

### 7.1 Very Large Telescope and SPHERE Adaptive Optics (AO) System

The high contrast images that will be analysed in this project were all taken by the European Southern Observatories (ESO's) Very Large Telescope (VLT)<sup>4</sup>. The VLT is a ground based imaging system with four Unit Telescopes, each with 8.2m apertures, and four movable Auxiliary Telescopes, each with 1.8m diameter. The telescopes can form a giant interferometer when operated together that is extremely powerful and can observe the smallest objects in the cosmos. When one of the Unit Telescopes is used individually it can observe objects as faint as magnitude 30 which is 4 billion times fainter than what the unaided eye can see. The telescopes can image across a broad wavelength region, from the ultraviolet region, around 300 nm, to the mid-IR region, around  $24\mu\text{m}$ . The VLT was successful in capturing the first image of an extra-solar planet and has imaged many protoplanetary disks.

The developments in adaptive optics (AO) in recent years has greatly improved the performance of large ground-based telescopes such as the VLT. Light from stellar objects is disturbed when it enters our atmosphere and this must be compensated for in ground-based telescopes in order to produce clear images. The primary objective in these processes is to correct for the effect of the atmosphere on light from celestial objects. Light from distant objects enters the Earths atmosphere and is affected by irregular fluctuations in properties of the atmosphere such as the temperature and density. These fluctuations, known as turbulence, leads to blurred

---

<sup>4</sup>Information about the VLT is sourced from <https://www.eso.org/public/ireland/teles-instr/paranal-observatory/vlt/>

images and the detail of the target cannot be seen. AO uses deformable mirrors controlled by computers to correct for the effect of the turbulence of Earth’s atmosphere in real-time.

One of the VLT’s adaptive optics systems is the Spectro-Polarimetric High contrast imager for Exoplanets REsearch (SPHERE). [Beuzit et al. \[2019\]](#) describes the rationale behind the development of SPHERE was to construct an instrument on a large telescope dedicated to high-image quality and high-contrast observation of bright targets. The primary scientific aim was to study exoplanet systems at large by providing an instrument capable of imaging outer giant planet population and circumstellar disks. The requirements for the apparatus was a significant contrast performance improvement allowing the detection capability in the planetary mass range, and the ability to obtain this on a large target sample. Additionally, the objective was to obtain exceptional image quality over a field-of-view large enough to study circumstellar disks, [Beuzit et al. \[2019\]](#).

When an image is taken of a star with a circumstellar disk, the image is saturated by stellar light and it is not possible to see any objects that may be near the star, such as the disk or any planets. The main mechanism used to reduce the amount of stellar light in the image are coronagraphs. Coronagraphs are physical masks placed in the aperture of the telescope positioned at the centre of the star. They physically block the stellar light from reaching the detector and reduce the amount of stellar light in the image, ensuring the image is not saturated. The coronagraphs do not block all the stellar light, meaning other post-processing techniques are required to remove the remaining stellar light and allow the disk scattered light to be seen.

## 7.2 Post-Processing Techniques to Remove Stellar Light from Images

This section summarizes the post-processing techniques for removing stellar light in images given in [Benisty et al. \[2023\]](#). Reference differential imaging (RDI) is the simplest technique. It involves a reference star being observed which has similar spectral properties and apparent magnitude to the scientific target. These observations are used to calibrate the instrument point spread function (PSF) and the reference star image is used to subtract the stellar light from the observation of the scientific target. Ideally the PSF should not change between the two observations, however it will likely change slightly due to the change in instrument and sky conditions. The advantage of this technique is that it does not reduce the throughput, or the intensity, of the signal from circumstellar disks and planets. The disadvantage of this technique is the possibility of over-fitting the data. This can occur when a bright circumstellar disk is observed, and this limits the throughput of the signal from the disk.

Other techniques are more commonly used in ground-based telescopes, the most widely used of these is angular differential imaging (ADI). This technique takes advantage of the apparent rotation of stars on the night sky when observed with an altitude-azimuth mounted telescope. A "de-rotator" is built into the telescope system to stabilise the image of the sky on the detector, this is turned off for ADI observations. Then the instrumental PSF and the central star being observed are kept stable while the off-axis stars, planets or disks appear to rotate and can be identified by this rotation. As the star remains in the same position in each of the images, it can be averaged across the images and subtracted. Then the images are rotated until the disk is pointing in the same direction in the images and they are combined together to give a final image of the circumstellar disk with no stellar light. ADI has the advantage of using the science data itself to determine the stellar light contribution, but comes with the issue of "self-subtraction". Self-subtraction occurs when the disk signal overlaps with itself on the detector and is removed along with the stellar light. The inclination of the disk affects how much self-subtraction might occur, disks which are observed face-on will result in the disk signal being almost entirely removed.

The most successful technique for circumstellar disk imaging is polarization differential imaging (PDI). Stellar light is unpolarized but when it scatters off the dust grains, it is partially linearly polarized. The scattering angle can range from  $0^\circ$  (forward scattering) to  $180^\circ$  (backward scattering). This scattering angle determines the degree of linear polarization of the stellar light. The instruments required are a polarizing or non-polarizing beam-splitter, polarization filters and a half-wave plate. The half-wave plate modulates the polarization direction of the light and splits it into two orthogonal, linearly polarized components. The star has only a low level of polarization, so the stellar light signal will be almost identical in both beams. The polarized light from the disk will differ between the beams, therefore different polarization filters are used to allow the light polarized in certain directions by the disk through and blocks the unpolarized light from the star. There is no temporal variation of the instrument PSF and no self-subtraction as in ADI.

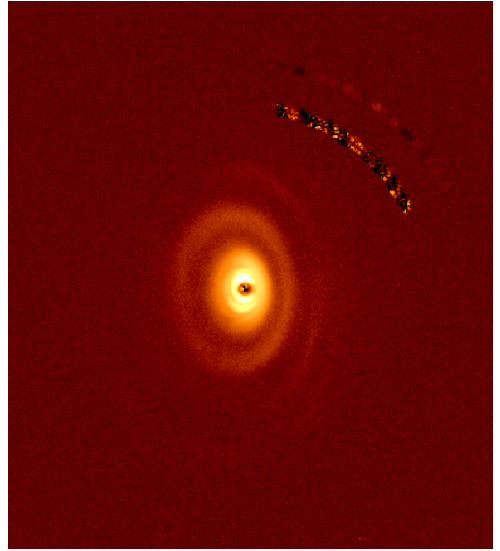
\*\*However, as the scattered light signal from the disk is only partially linearly polarized, very faint disk structures (mostly at large angular separations from the star), might not be detected with high signal-to-noise ratio, or in some cases at all. Furthermore the technique is typically no suitable to detect embedded planets as their thermal emission is unpolarized.

### 7.3 High Contrast Image Example

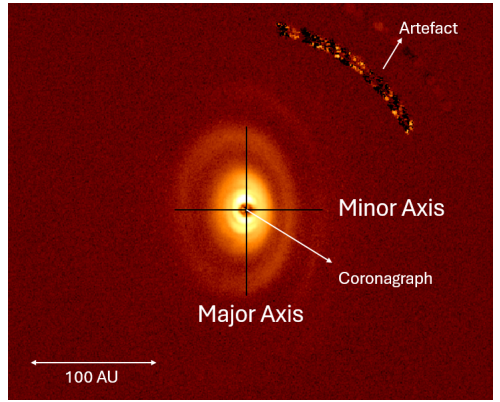
Figure 8 shows one of the high contrast, polarized light images that will be used in this project. This is an image of the disk around HD97048. It is possible to make out the 4 rings and corresponding gaps in the disk, compared to in figure 4 where only 2 rings were visible. The focus of this project is to find which disks are bright, to deduce this it is necessary to measure the brightness of some disks directly. This will provide a category of disks which we know are bright and these can be used for comparisons. The brightness can be measured directly from the scattered light images, however when the disk is viewed under inclination, the "bowl-shaped" surface of the disk produces offsets of disk structure and its brightness along the minor axis, [Benisty et al. \[2023\]](#).

Figure 9 below shows the same image with labels to indicate the major axis, minor axis, artefacts in the image, size scale and the coronagraph. There is clearly an offset in the structure of the disk along the minor axis. This is due to the scattering angle of the light from the disk. The disk has a near-side and far-side with respect to the detector.

The side of the disk which is brighter is the near-side as the light is forward scattered from this side. Light from the far-side of the disk is backward scattered. This causes the disk brightness to change significantly along the minor axis. The elliptical shape of the disk is due to the disk inclination. The brightness offset appears dominantly along the minor axis because of the flaring geometry of the disk. Therefore, the brightness must be measured along the major axis of the disk where there is much less significant change in the structure and brightness of the disk. The coronagraph appears as a black circle in the centre of the image where the star should be, there are no photons detected in this part of the image.



**Figure 8:** High Contrast Image of the disk around HD97048.



**Figure 9:** High Contrast Image of HD97048 with labels indicating the major axis, minor axis, artefacts in the image, size scale, and the coronagraph.

## 8 Project Outline

The overall aim of this project is to establish a method to accurately predict the brightness of circumstellar, protoplanetary disks. This is achieved through using photometric catalogue data from the WISE Satellite mission along with high-contrast images. The project has two main objectives: (i) To formulate a connection between the brightness determined from the photometric data from the WISE to the brightness measured from the high contrast images. (ii) Using this connection, make predictions for which disks should be bright and use this to suggest a new sample of disks that should be selected as future targets for high contrast imaging with the ESO's VLT.

A sample of 52 systems will be analysed by first finding the photometric data for the disk from the WISE catalogue in the VizieR database and then directly measuring their brightness from high contrast images obtained with the VLT. The WISE catalogue can be queried in Python to find the magnitude measurements for each of the disks in the four WISE bands. The magnitudes will be converted to flux density and the slopes between the WISE bands are found to show how the flux density is changing throughout the disk. The change in flux density at the short wavelengths will correspond to the inner region of the disk and the change at the longer wavelengths corresponds to the outer disk region. The prediction for bright disks is a decrease in flux density from the inner disk region due to the presence of a large cavity which permits strong illumination of the whole disk by the stellar light. There should also be an increase in flux density from the outer disk region indicating there is disk material that will scatter the light and thus, the disk structure will be visible in the image. Therefore, disks with negative slopes from the WISE 1 ( $3.35\mu m$ ) to WISE 3 ( $11.6\mu m$ ) band, and positive slopes from the WISE 3 to WISE 4 ( $22.1\mu m$ ) band will be predicted to be bright in scattered light images.

To determine if this prediction is accurate, the brightness of the disks in the sample will be directly measured from high-contrast images. Photometry will be performed on each of the images to extract a single brightness ratio that can be compared to the WISE slopes. This will show if the disks that were predicted to be bright from their WISE slopes are confirmed to be bright in scattered light. The ratio will be independent of the central star flux which always comparison between disks.

If the results show a correlation between the disks that are measured as bright from images having the expected WISE slopes, the method will be applied to disks which have yet to be imaged. The WISE slopes will be calculated for all the appropriate systems observable with

the VLT. Those which have negative slopes between WISE 1 and WISE 3, and positive slopes between WISE 3 and 4 will be predicted to be bright. This sample can be put forward as future targets for high contrast imaging by the VLT. This would provide a new range of images in which the disk structure should be clearly seen and used to reveal information about planets that could possibly be forming in these disks. By predicting which disks are bright prior to making observations, it optimizes telescope observation time by increasing the chance of obtaining images that we can use to further our understanding of planet formation.

## 9 Methodology

### 9.1 Sample

A sample of disks with known brightness are required for analysis to determine how the brightness of disks can be predicted. The sample in this work consists of 18 Herbig stars and 34 T Tauri stars. VLT/SPHERE observations are used to directly measure the brightness of their circumstellar disks. These 52 stars have masses ranging from  $0.4\text{-}3.0 M_{\odot}$ , covering a wide range of intermediate and low-mass stars. The brightness of the disks will be compared to the change in flux density detected from the disk, which is obtained from the WISE database.

The disks vary significantly in appearance in scattered light images. Each disk has unique spatial extent and morphology but the disks can be classified into categories. Classification based on structure is not significant in this work, disks fall into either bright or faint categories. Faint disks can be separated further. Disks that are faint, they give off very low signal and have no visible features. Disks that are small; signal detected is on a very small scale, and shadowed disks. A high amount of flux is measured in the SEDs of these disks but they are shadowed in scattered light images due to material close to the star blocking the stellar light from illuminating the rest of the disk.

### 9.2 Predicting Brightness of Disks from WISE Flux Excesses

#### 9.2.1 WISE Slopes

The WISE satellite measured the magnitude from circumstellar disks around young stars in four wavelength bands. This provides four data points that can be plotted to illustrate a partial SED. The slopes between the points can be found to show how the flux density changes throughout

the disk. This is achieved by calculating the difference in flux density from  $3.35\mu m$  (WISE W1 band) to  $11.6\mu m$  (WISE W3 band) and from  $11.6\mu m$  to  $22.1\mu m$  (WISE W4 band). The calculated values are listed in Table 3.

The WISE data is found in the *VizieR* library and the WISE data for each disk is extracted from the database using Python, specifically using a package called *astroquery* from the *astropy* module. The WISE catalogue is selected, and each star can then be searched within this by querying the catalogue with the star name. A small region around the star must be defined in order to ensure the data retrieved corresponds to the source. By defining the region around the target as 2 arcseconds, this ensures only data for that star is given. The magnitudes values in each of the WISE bands are extracted for each disk in the sample and must be converted to flux density before calculating the slopes that will be used to predict the disk brightness.

### 9.2.2 Converting WISE Magnitudes to Flux Densities

The four magnitudes for the disk are obtained from the WISE data table using the column names 'W1mag', 'W2mag', 'W3mag', and 'W4mag', and then converted to flux values. The flux density, in units of Janskys (Jy), is computed from the WISE magnitudes,  $m_{vega}$ , using:

$$F_\nu[Jy] = F_{\nu 0} \times 10^{(-m_{vega}/2.5)} \quad (4)$$

$F_{\nu 0}$  is the zero magnitude flux density corresponding to the constant that gives the same response as that of Vega. The zero magnitude flux density for each WISE band is given in Table 1. The flux density must be multiplied by the frequency of each of the WISE bands to give the flux, in  $Wm^{-2}$ . The frequencies of each of the WISE bands are given in Table 1.

The slope between the flux density points must be calculated on a log scale, as a wide range of magnitudes is covered. The slope between two WISE bands is found using:

$$Slope = \frac{\log(\nu F_{\nu 1}) - \log(\nu F_{\nu 2})}{\log(\lambda_1) - \log(\lambda_2)} \quad (5)$$

The SEDs for a bright disk (GM Aur) and a faint disk (CI Tau) are seen in figure 10. The black line indicates the blackbody curve for the star and the red data points correspond to the flux detected from the disk. In the near-IR and mid-IR regions the flux from the star is decreasing significantly and the curve has a very steep negative slope. When material is present in a circumstellar disk, this slope increases, but remains negative in most cases, due to the extra flux being detected from the disk. Therefore, for most disks the slope between W1 and W3 will be negative but this does not mean every disk has a cavity in its inner region. Disks with large

**Table 1:** Zero magnitude flux density ( $F_{\nu 0}$ ) and frequency ( $\nu$ ) for each WISE band

Band	$F_{\nu 0}$ [Jy]	$\nu$ [GHz]
W1	309.540	$8.95 \times 10^4$
W2	171.787	$6.52 \times 10^4$
W3	31.674	$2.59 \times 10^4$
W4	8.363	$1.36 \times 10^4$

inner cavities will have a more steep negative slope, due to a significant decrease in material present in the inner disk. This is illustrated by the SED for GM Aur, there is a significant decrease in energy in the near-IR to mid-IR region due to the cavity present in the disk. The slope from W1 to W3 is steep and negative. There is a significant increase in flux detected at the longer wavelengths due to the presence of material in the outer region of the disk. This is shown by the positive slope between W3 and W4.

Comparing this to the SED for the faint disk CI Tau, the slope between W1 and W3 is still negative but it is significantly less steep. There is much more flux detected at the short wavelengths from this disk which shows that there is a lot of material in the inner region of this disk which will cause the disk to be shadowed. There is also a decrease in flux detected at the longer wavelengths which suggests that this disk may be small, making it more difficult to resolve in images.

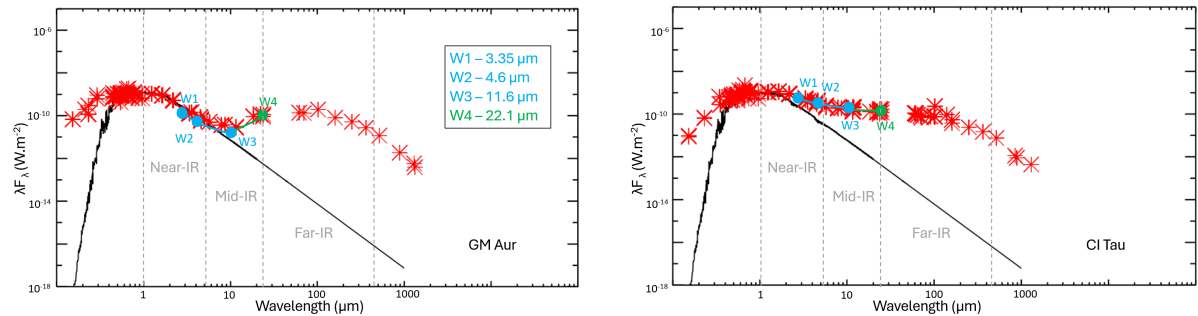


**Figure 10:** Schematic representation of the SEDs for a bright disk, GM Aur, and a faint disk, CI Tau (Garufi et al. [2024]). The WISE flux points and the slopes between the four bands are added.

The slopes between the four WISE bands can be used to identify the shape of the SEDs for the disks in the sample. Bright disks are expected to have a large decrease in flux density at shorter wavelengths, typically around  $10\mu m$ , this is indicated by a steep negative slope between WISE 1 and WISE 3 bands. Disks with this geometry point towards disks with large cavities and thus, disks which should be bright in scattered light. It is also expected that these disks

have a subsequent positive slope between W3 and W4. This corresponds to longer wavelengths and shows the disk has material in its outer region that is emitting energy at these wavelengths and will scatter the stellar light allowing the whole disk to be visible in the image. These slopes will be compared to the directly measured brightness to ascertain if the predicted brightness is accurate.

## 9.3 Directly Measuring Brightness of Disks from High Contrast Images

### 9.3.1 High Contrast Observations

The observations analysed in this project were obtained by the VLT and the SPHERE adaptive optics system. The images are mainly polarimetric, coronagraphic images, the coronagraph used in the system is a classical Lyot coronagraph. For images where a coronagraph was not used, a mask must be added before measuring the brightness to prevent the stellar light being included in the measurement, (e.g. GG Tau). The observations were carried out in three different wavelength bands; 32 targets were imaged in the H band (centered at  $1.625\text{ }\mu\text{m}$ ), 12 in the J band (centered at  $1.245\text{ }\mu\text{m}$ ), and 9 in the K band (centered at  $2.182\text{ }\mu\text{m}$ ). After basic science reduction is completed on the images, the disk around the star is still not visible. Therefore, post-processing techniques, such as polarimetric differential imaging (PDI), are used to subtract the bright stellar light that dominates the image. The images were processed with the IRDAP pipeline which carried out basic cleanups and processing, as well as the PDI.<sup>5</sup>

### 9.3.2 Aperture Placement

The images are stored as fits files which can be opened and displayed in Python. A log scaled colourmap allows the disk to be visualised best. The image on the left in Figure 11 shows the disks around HD97048, GG Tau, HD100546, and TW Hya as displayed in python. It is clearly seen for HD97048, GG Tau and HD100546 that the brightness of the disks are not uniform, there is an offset along the minor axis due to the inclination of the disks and the scattering of the light from different parts of the disk, as discussed in section 7.3. For TW Hya there is no offset in the brightness as this disk is observed face-on; the disk is not inclined with respect to us and the light is scattered at the same angle at each point in the disk. The brightness of each disk must be measured along the major axis as the offset in the brightness is least significant along this axis. To achieve this a number of circular apertures must be placed along the major

---

<sup>5</sup>IRDAP website: <https://irdap.readthedocs.io/en/latest/>

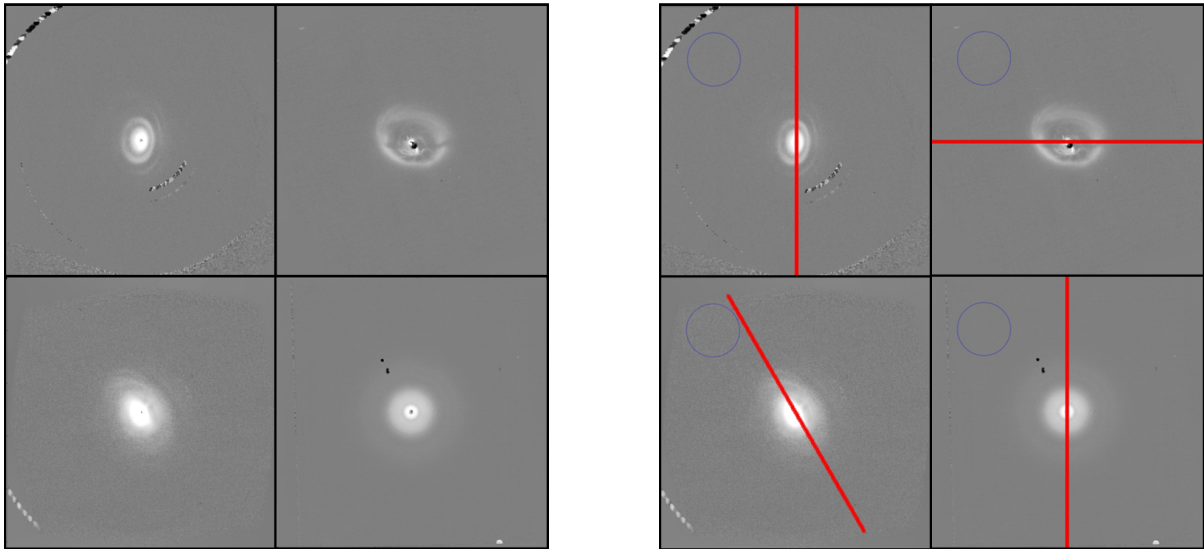


**Figure 11:** High contrast images of the disks around HD97048, GG Tau, HD100546, and TW Hya, as displayed in python. The same images with apertures plotted to indicate the major axis along which the surface brightness is measured.

axis in the image and each one will measure the surface brightness contained within that radius. Each disk must be carefully looked in order to determine the angle of the major axis and thus, where the apertures should be placed. In the majority of the images, the major axis follows the largest extent of the disk. Once this is determined apertures are placed at equal distances apart along the axis and the coordinates for the location of each aperture is found. The image on the right in Figure 11 shows the apertures plotted along the major axes for four disks. Aperture photometry must be performed to find the surface brightness detected from the disk at each aperture. Circular apertures are placed at evenly spaced coordinates along the major axis of the disk and the mean surface brightness within the aperture is extracted.

### 9.3.3 Background Noise Calculation

It is important to ensure only the disk surface brightness is being measured in the image and not the background noise. The pixels in the image vary in brightness due to the noise in the detector. If the signal from the disk is close to the level of the noise, it is very difficult to distinguish if disk signal or noise is being detected. The noise must be measured in a region of the image where there is clearly no disk signal. The surface brightness that is measured from the noise will range slightly above and below zero, therefore, a large aperture is used to measure the standard deviation of pixel values in the background limited region of the image. The noise is set equal to three times the standard deviation to guarantee only the disk signal is being measured. As

the surface brightness for the disk is measured in each of the apertures, it is checked against the noise level. If the surface brightness reaches the level of the noise the measurement is discarded. This allows the disk surface brightness to be measured out to the edge of the disk and ensures the noise is not included in the measurements.

### 9.3.4 Calculation of Disk Brightness in Scattered Light

The disk brightness in scattered light is given by the brightness ratio  $\delta_{pol}$ . This can also be referred to as polarized-to-stellar light contrast, as the light from the disk is polarized and the brightness of this is being measured relative to the stellar flux, which is un-polarized light. In this way the dependence of the disk surface brightness on the amount of stellar flux it receives is cancelled. The scattering phase function ([Mulders et al. \[2013\]](#)), the disk extent, and the disk inclination all affect the amount of light scattered from the disk. Computing the average of the surface brightness value from the inner to the outer radius, along the major axis, significantly mitigates these dependencies. It is also required to account for the separation of the apertures from the center of the disk by normalizing each separation by the distance squared, [Garufi et al. \[2017\]](#). To summarise, the disk surface brightness ratio can be found using, [Garufi et al. \[2022\]](#):

$$\delta_{pol} = \frac{1}{r_{out} - r_{in}} \cdot \int_{r_{in}}^{r_{out}} \frac{F_{pol}(r) \cdot 4\pi r^2}{F_*} dr \quad (6)$$

A surface brightness profile is plotted for each disk to show how the brightness varies out from the center of the disk. The surface brightness  $F_{pol}$  is measured along the major axis and plotted as a function of the aperture index in pixel values. The brightness of light scattered from the disk decreases as a function of  $r^2$ , where  $r$  is the distance from the center. Further out in the disk the light from the central star is spread over a larger shell, therefore less light is scattered from the outer regions of the disk. To correct for this, the surface brightness in each aperture is multiplied by  $4\pi r^2$ , where  $r$  is the distance to the aperture from the center of the image. The surface brightness is measured in  $Jy/arcsec^2$ , therefore the distance must be in arcseconds. The distance of each of the apertures is measured in pixels and converted to arcseconds by multiplying by 0.012251 arcseconds/pixel, the pixel scale constant. The brightness is plotted against the aperture distances to create another brightness profile. The brightness is averaged from the center of the disk to the outermost radius with detectable signal ( $r_{out}$ ) to give a single brightness value for the disk.

However, the brightness of the disk must be given relative to the brightness of the central star,  $F_*$ . This is because a disk can appear bright in images due to the central star being

particularly bright and it strongly illuminates the disk that would appear faint without this strong illumination. By dividing by the stellar flux, this dependency is cancelled out and this allows comparison between disks around stars with different brightness. The stellar fluxes can be found using the same method for finding the WISE magnitudes. The Two Micron All Sky Survey (2MASS) was an astronomical survey conducted of the entire sky at near-infrared wavelengths. The 2MASS catalog contains the stellar fluxes for millions of point sources, including the sample of this project. The catalog is queried in VizieR within a region of 2 arcseconds and the magnitude of the star is extracted using the band filter taken from the image file name. The magnitude,  $m_{2mass}$  is converted to flux in  $Jy$  using:

$$F_{Jy} = F_0 \times 10^{-0.4 \cdot m_{2mass}} \quad (7)$$

where  $F_0$  is the zero magnitude flux, given for each band in Table 2. The brightness of the disk measured from the image is divided by the stellar flux to give the disk brightness ratio in scattered light. The brightness ratios for the sample are listed in Table 3 and can be compared to the WISE slopes to judge the accuracy of the prediction for bright disks.

*Table 2: Values from VIZIER conversion table for filters, matching best 2MASS filter properties*

Band	$F_0$ [Jy]	Uncertainty Order [Jy]
$F_{0J}$	$2.001 \times 10^3$	$0.027 \times 10^3$
$F_{0H}$	$1.562 \times 10^3$	$0.017 \times 10^3$
$F_{0K}$	$6.650 \times 10^2$	$0.035 \times 10^2$

## 10 Results and Discussion

### 10.1 Classification of Sample into Bright or Faint Disks

This work uses the threshold definition for bright disks of  $\delta_{pol} < 3 \times 10^{-3}$  as in [Garufi et al. \[2024\]](#). Out of the 52 disks in the sample, 22 lie below this threshold and are classified as faint. However, some of these disks are bright in scattered light images. The category of faint disks can be separated between sources where the disk is visible in the image and the disk geometry can be inferred, and sources where the disk signal is scarcely detected and the structure is not visible. Seven disks fall into the first subcategory and the fifteen other disks have no structure visible in the images. Figure 12 displays an example of a faint disk, CI Tau. There is very little disk signal detected. The bright yellow hue in the center of the image is the light scattered from the disk. The disk has no observable structure.

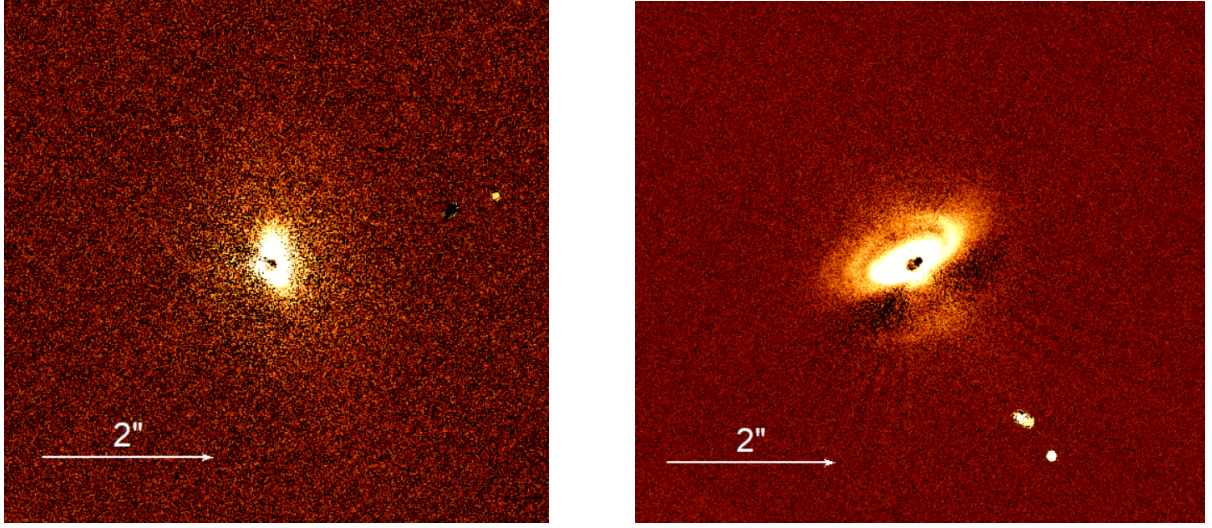


**Figure 12:** Comparison of scattered light images of a faint disk (CI Tau) and a bright disk (HD34282). The disk around CI Tau is very small in the image and no structure is visible. Whereas, the disk around HD34282 has clear structure, a ring and gap is visible.

The other 34 disks have brightness values above the threshold and are considered bright disks. They are all visible in scattered light images and show evidence of substructures. There is huge diversity in the bright disks, some feature spiral arms, such as CQ Tau.

Figure 13 presents HD34282, it is a bright disk with visible rings and gaps. The disk is also inclined allowing the mid-plane of the disk to be visible in the image. The disks around HD142527 and AB Aur, are massive and show large cavities, shadows, and asymmetric spirals. Many bright disks such as TW Hya, and HD97048 feature multiple symmetric rings and gaps. Others show one ring around a cavity, such as PDS 70.

Figure 15 depicts the scattering geometry of inclined disks. Light that is scattered from the near-side of the disk is forward scattered (through an angle  $< 90^\circ$ ), this means there is more light scattered from this side of the disk than other regions of the disk. There is less light scattered through  $90^\circ$  and from the far-side of the disk, which is backward scattered (through an angle  $> 90^\circ$ ). Light that is scattered from disks that are very inclined with respect to us is going to be dominated by forward scattering as the majority, or possibly all, of the light in the image will be from the near-side of the disk.

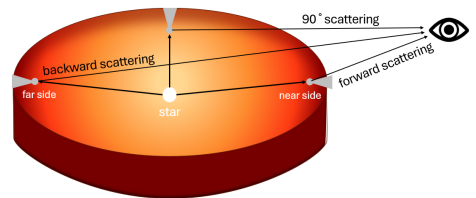


**Figure 13:** Schematic representation of the scattering geometry of a circumstellar disk.

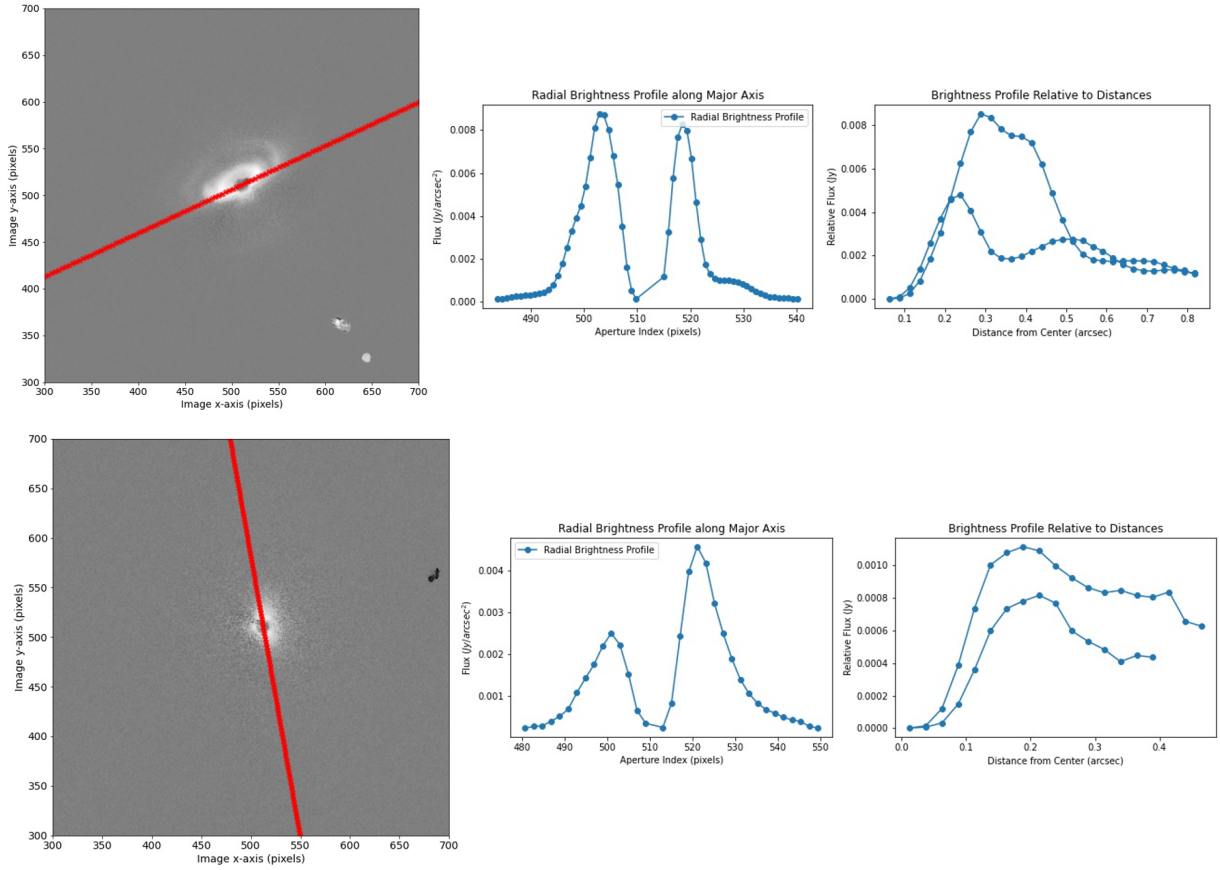
## 10.2 Brightness Profiles

Figure 14 shows an example of two images with apertures plotted along their major axis and the corresponding brightness profiles before and after being corrected by the distance of the apertures. The image and brightness profiles on top are for HD34282, this is a bright disk. The disk and its structure is visible in the image and the brightness profiles also highlight a ring and gap that are present in the disk. The brightness profile shows two peaks, the highest corresponds to the centre of the disk and the other peak show the increase in flux that is detected from the ring that is seen in the image. There is only one peak for the ring, instead of two peaks that would indicate a symmetric ring around the disk. This is due to the disk inclination, the ring is only visible at one side, the far-side of the disk. Light from the near-side is so bright it prevents the ring being detected. The flux decreases significantly between the central peak and the next two peaks indicating the gap present in the disk. There is a cavity present in the disk that is not resolved in the image as it is so close to the central star, it is also not seen in the brightness profile. However, the stellar light is able to illuminate the disk due to the cavity, which allows the structure of the rings and gaps to be visible in the image. These are the types of disks we want to image more as their structure can be seen in scattered images and they can be studied to identify if planets may be forming in these disks.

The image and brightness profiles on the bottom of figure 12 are for CI Tau, a faint disk. The disk is barely visible in the image and the brightness plot shows how much less flux is detected from this disk as compared to HD34282. The brightness profile features two peaks, suggesting there may be a sub-structure present in the disk such as a spiral arm, however it is not resolved in the image.

## 10.3 Comparison of Disk Brightness with WISE Slopes.

A histogram of the brightness ratios for the sample is shown in Figure 16. The 22 faint disks lie below  $3 \times 10^{-3}$  as expected. 30 disks lie above the threshold, with 5 of these having very high brightness ratios due to their inclination. Table 3 presents all the data generated for the sample of disks in this work. The source name, slopes between WISE bands and disk brightness are given. By comparing the disk brightness to the WISE slopes, a relationship can be established to show how the flux measured by WISE can be used to predict if the disk is bright or faint. HD34282 has a slope of -1.10 between the WISE 1 and 3 bands. This spans the shorter wavelengths and the  $10\mu\text{m}$  region and exhibits the decrease in material in the inner region of the disk due to a large cavity. This leads to a decrease in flux detected as there is very little material emitting



**Figure 14:** (a). High Contrast Image of HD34282, a bright disk, with apertures plotted along the major axis, radial brightness profile plotted as a function of aperture index, and distance corrected radial brightness plotted as a function of distance from the center of the image. (b). High Contrast Image of CI Tau, a faint disk, with apertures on the major axis, radial brightness profile as a function of aperture index, and distance corrected radial brightness as a function of distance from the center of the image.

energy at these shorter wavelengths. The disk has a slope of 0.485 between the WISE 3 and 4 bands pointing towards a subsequent increase in flux detected at longer wavelengths due to an abundance of material further out in the disk. A disk brightness of  $9.19 \times 10^{-3}$  was measured from the high contrast image for the disk, confirming that this is a bright disk and the structure of the disk is clearly visible in the image, allowed by the presence of the large cavity which is shown by the WISE slopes.

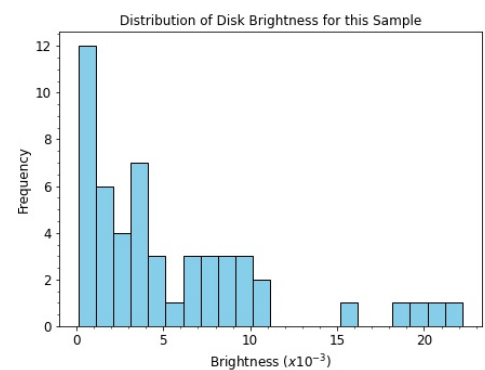


**Figure 15:** Histogram of Disk Brightness Ratios for the Sample.

**Table 3:** Sources, WISE slopes and disk contrast values.

Source	W1-W3 Slope	W3-W4 Slope	Disk Brightness ( $10^{-3}$ )	$M_{dust}/M_*(\times 10^4)$
HD31648	-0.386	-0.871	0.536	$0.82 \pm 0.04$
HD34282	-1.10	0.485	9.19	$1.19 \pm 0.22$
HD36112	-0.996	0.215	2.60	$0.30 \pm 0.05$
HD97048	-0.152	0.811	3.53	$1.33 \pm 0.10$
HD100453	-0.383	0.947	3.48	$0.50 \pm 0.05$
HD100546	0.794	1.04	8.78	$0.60 \pm 0.03$
HD135344b	-1.88	1.68	4.67	$0.58 \pm 0.08$
HD139614	-0.072	0.958	1.45	$0.98 \pm 0.06$
HD142527	-0.669	-0.023	7.50	$4.15 \pm 0.11$
HD142666	-0.303	-0.675	0.497	$0.54 \pm 0.04$
HD143006	-1.54	0.958	1.19	$0.26 \pm 0.02$
HD144432	-0.225	-0.581	0.142	$0.17 \pm 0.04$
HD163296	-0.510	-1.16	1.64	$0.84 \pm 0.02$
HD169142	-0.409	1.63	2.63	$0.66 \pm 0.05$
HD179218	0.545	-0.315	1.74	$0.28 \pm 0.03$
TW Hya	-0.930	1.25	7.74	$2.29 \pm 0.10$
PDS 70	-1.12	0.305	6.35	$1.60 \pm 0.02$
EM* SR21	-0.473	2.07	5.42	$0.26 \pm 0.03$
LkCa15	-1.51	-0.023	3.54	$2.01 \pm 0.07$
V4046 Sgr	-1.23	1.27	2.55	$0.61 \pm 0.06$
PDS 66	-0.970	0.473	1.68	$0.93 \pm 0.03$
GM Aur	-1.13	2.07	20.8	$3.36 \pm 0.15$
RX J1615.3-3255	-1.09	1.02	4.37	$2.71 \pm 0.08$
V1247 Ori	-1.29	1.76	4.62	$0.92 \pm 0.12$
T Cha	-1.96	-0.060	9.84	$0.65 \pm 0.09$
DoAr 44	-0.758	0.514	3.76	$0.79 \pm 0.08$
DZ Cha	-0.123	0.820	2.90	$<0.17$
AS 209	0.135	0.054	0.748	$1.97 \pm 0.19$
IM Lup	-1.01	-0.419	10.5	$3.19 \pm 0.11$
MY Lup	-0.726	0.273	18.2	$0.61 \pm 0.04$
RU Lup	-0.481	0.005	0.681	$4.09 \pm 0.14$
RY Lup	-0.942	0.148	15.9	$0.44 \pm 0.03$
CI Tau	-1.05	-0.269	1.42	$2.27 \pm 0.20$
CQ Tau	-0.253	0.693	8.13	$0.96 \pm 0.01$
CS Cha	-2.07	3.14	3.80	$1.77 \pm 0.63$
CV Cha	-0.967	-0.075	0.604	$0.09 \pm 0.01$
Sz 111	-2.44	1.53	6.53	$2.52 \pm 0.25$
DI Cha	-1.07	-2.28	0.112	$0.16 \pm 0.04$
IRAS 08267-3336	-0.491	0.497	22.2	0
SY Cha	-0.628	0.098	1.05	$0.95 \pm 0.04$
VZ Cha	-1.03	-0.098	0.366	$1.47 \pm 0.01$
EX Lup	-0.094	0.027	0.325	$0.62 \pm 0.13$
SZ Cha	-1.48	1.46	8.86	$0.63 \pm 0.16$
GW Lup	-0.793	-0.146	0.239	$5.34 \pm 0.90$
J16083070-3828268	-2.58	3.77	19.4	$0.40 \pm 0.01$
V718 Sco	-0.098	-0.921	0.327	$0.24 \pm 0.02$
GG Tau	-1.04	-0.043	10.9	$10.16 \pm 0.90$
UX Tau	-1.92	2.06	8.37	$0.41 \pm 0.01$
LkHα330	-1.54	1.35	3.90	$0.53 \pm 0.02$
AB Aur	-0.926	0.357	9.26	$0.33 \pm 0.03$
Ak Sco	-0.938	-0.0018	3.59	$0.09 \pm 0.01$
J18521730-3700119	-1.46	2.39	6.65	$0.95 \pm 0.12$

Comparing this to CI Tau; this disk has a slope of -1.05 between the WISE 1 and 3 bands and a slope of -0.269 between the WISE 3 and 4 bands. The flux detected from the disk decreases significantly across the four WISE bands. This indicates that this is a small disk and thus, it will appear small in the image and its structure cannot be resolved. The disk is classified as faint, confirmed by the directly measured disk brightness of  $1.42 \times 10^{-3}$ .

Analysing the slopes between the WISE bands gives the trend in the flux that is emitted from disks; it does not give the absolute value of the emission relative to the stellar emission. It can be seen from looking at the SED for CI Tau in section 9.2.2, that although CI Tau has a negative slope between the WISE 1 and WISE 3 bands, the absolute flux detected is still higher than that for the bright disk, GM Aur. This shows that there is material present in the inner region of the disk that would cause the disk to be shadowed. The negative slope across the four bands is what shows us that this disk is faint in scattered light images.

HD179218 is another disk that appears faint in the scattered light image. It has a disk brightness of  $1.74 \times 10^{-3}$ . The change in flux between the WISE 1 and 3 bands is 0.545 and between the WISE 3 and 4 bands is -0.315. The slope between the first two bands is positive which implies there is substantial disk material in the inner region which will shadow the disk. The negative slope between the last two bands demonstrates an absence of material in the outer region of the disk. This disk is similar to CI Tau, it is shadowed and it is too small to resolve in images. This may also be a system that is still embedded in material left over from when the star formed from a giant molecular cloud. This is indicated by the slopes being relatively close to zero in both cases, that is, the slope is almost flat across the four bands.

## 10.4 Disk Dust Mass

Disk dust mass is another factor that significantly affects if a disk appears bright in scattered light images. The disk must contain a large enough amount of dust grains to scatter enough light that can be detected and allows the disk and its structure to be seen in images. A disk may have the correct geometry that points towards it being bright but if there is not a high enough dust mass, there won't be enough light scattered for the disk to appear bright in the image. Similarly, the WISE slopes for a disk may predict a disk to be faint but if there is a very large amount of dust grains present in the disk, they can scatter enough light to allow the disk structure to be visible when observed. To take this into consideration, the disk dust mass relative to the stellar mass for all the disks was sourced from [Garufi et al. \[2018\]](#), these values are listed in Table 3.

This significance is illustrated by HD142527. It has WISE slopes of -0.669 between W1 and W3 and -0.023 between W3 and W4. Similar to CI Tau and HD179218, this disk would be predicted to be faint, however it has a brightness ratio of  $7.50 \times 10^{-3}$ . This is due to the very high dust mass of  $4.15 \times 10^4$ . There is enough dust grains in the disk to scatter enough light to allow this disk to be bright in images.

The WISE slopes of the whole sample and the disk brightness is shown below in Figure 17. The slope between W1 and W3 is plotted on the x-axis, the slope between W3 and W4 is plotted on the y-axis and the brightness is represented by the colour gradient. The disk dust mass is encoded in the size scale of the data points. There is an apparent trend in the brightness of the disks and their WISE slopes. All the disks except three have negative slopes between W1 and W3 as expected, but the majority of the bright disks have a much larger negative slope than the faint disks. This is due to there being very little material in the inner region of the disks due to a large cavity which allows the stellar light to illuminate the entirety of the disks and they appear bright in scattered light images. The brightness of the disks increases as the slope between W1 and W3 becomes more negative. This is in line with our expectations that bright disks are predicted to have steep negative slopes between these bands.

The brightness of the disks also increases as the slope between W3 and W4 becomes more positive. The majority of the faint disks have negative slopes between these bands indicating there is not a lot of material present in the outer regions of the disks which typically means the disks are too small to be resolved in images and there is not enough dust grains to scatter enough light that can be detected. Most of the bright disks have positive slopes between these bands, and the brightness appears to increase as the slope becomes more positive. This is showing that these disks which have less material in the inner region of the disk, which then show an increase in material in the outer regions, indicated by the positive slope, will be bright in scattered light images. The stellar light is able to illuminate the outer regions and there is enough dust present to scatter sufficient light that the disk structure is visible in observations.

The diagram shows some exceptions to the trends for bright disks and faint disks. However, these can be explained by analyzing Table 3, the images for the disks and taking some other factors into consideration. Figure 16 shows there are five disks that are measured as bright according to their brightness ratio but do not have the expected WISE slopes. HD142527, PDS 70, LkCa15, and GG Tau have slope values that predict they should be faint but have brightness ratios above the threshold for bright disks. These disks appear very bright in the images due to the very large dust mass they feature. IM Lup has negative slope across the four WISE bands but is measured to be very bright. This is because this disk is very inclined and therefore

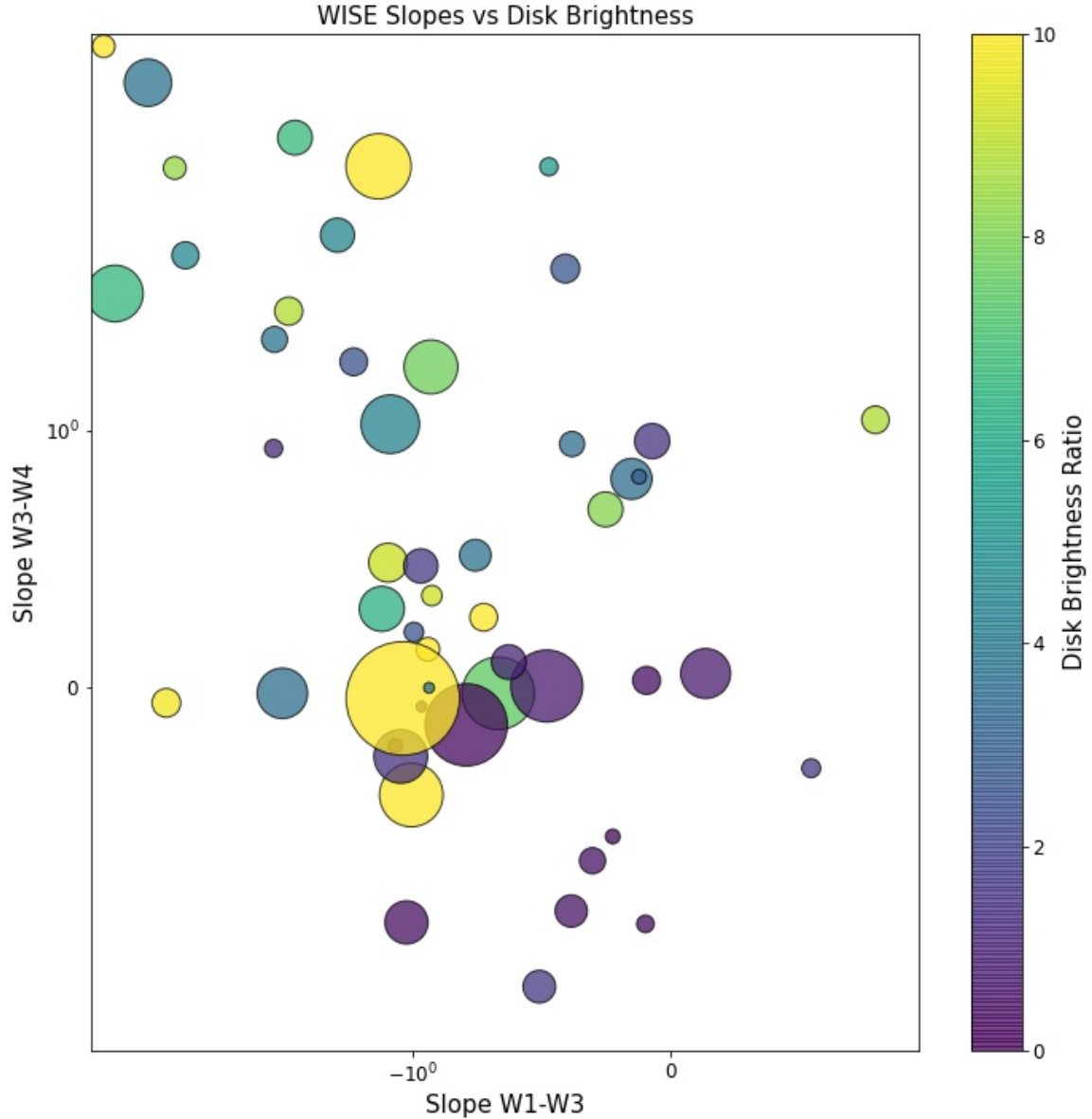


**Figure 16:** Plot of WISE Slopes vs Disk Brightness. Slope between W1 and W3 is plotted on the x-axis. Slope between W3 and W4 is plotted on the y-axis. Colour distribution corresponds to brightness of disk, size scale indicates disk dust mass.

the majority of the light from this disk is forward scattered which introduces a bias into the measurement of its brightness as explained previously.

There are also outliers in the trend for faint disks. The figure and data table show nine disks which have WISE slopes that would predict them to be bright; HD36112, HD139614, HD143006, HD169142, V4046 Sgr, PDS 66, DZ Cha, SY Cha, and EX Lup. These disks all have disk dust mass  $< 1 \times 10^4$  which means there is not enough dust grains present in these disks to scatter enough light to allow them to be bright in scattered light images.

These outliers show how critical the dust mass is for allowing disks to scatter enough light

that their structure can be seen in images. The figure illustrates the importance of the geometry of the disks, that we can predict using the WISE slopes, for the stellar light to illuminate the whole disk. A good example of this is the disk that is plotted in the very upper left corner of the figure. This is J1608-3070, it has a very steep, negative slope between W1 and W3, indicating a large cavity present in the disk. It also has a very steep, positive slope between W3 and W4, showing there is a lot of material present in the outer region of the disk. The disk is measured to have a very high brightness ratio of  $8.37 \times 10^{-3}$ , although it has a low dust mass of  $0.41 \times 10^4$ . This shows that while there is not a significant amount of dust grains in this disk, the presence of a large cavity allows enough stellar light to strongly illuminate the entirety of the disk and thus, its structure can be seen in the scattered light image.

Overall, Figure 16 demonstrates that disks that have very steep negative slopes between W1 and W3, and positive slopes between W3 and W4 are bright in observations. Exceptions to this trend are due to disks which have a low dust mass that cause them to be faint in the images. The faint disks generally have negative slopes across both W1-W3 and W3-W4, with the exception of disks which have high dust mass or are very inclined, these disks will appear bright when observed.

## 10.5 Finding a New Sample of Disks to Image

A relationship between the WISE slopes and the disk brightness has been established from the findings outlined above. The prediction is that disks which have steep negative W1-W3 slope and positive W3-W4 slope should be bright in scattered light images. The steep negative W1-W3 slope indicates a cavity is present in the disk which allows the disk to be illuminated. Using this result, the aim is to find a new sample of disks which are predicted to be bright and should be imaged.

### 10.5.1 Constraints for Finding New Sample of Disks

To find a new sample of interesting systems to observe with the VLT and SPHERE, there are several constraints that are required for the systems to be observable. These are used first to form a range of systems that can be observed with the VLT and then the WISE slopes for this range will be determined.

The VLT is located in the southern hemisphere, therefore the systems must be visible from this hemisphere, i.e., they must have a declination<sup>6</sup> smaller than 30 deg. The central star in the

---

<sup>6</sup>Declination is the angular distance north or south from the celestial equator.

system must be bright enough at short optical wavelengths to feed the adaptive optics system. Therefore, the Gaia magnitude from the Gaia Satellite Mission (or the G magnitude), must be smaller than 13.5 mag<sup>7</sup>. Lastly, the stars must be close enough that their disks can be resolved in the images. The ideal distance for high resolution is 200 parsecs<sup>8</sup>, but we can go out to 500 pc to capture as many interesting systems as possible. In the catalogs parallax is listed rather than distance, but the distance can be found using:

$$distance(pc) = \frac{1000}{parallax(mas)} \quad (8)$$

where parallax is measured in milli-arcseconds.

The Gaia catalog is queried with these constraints to find the systems that meet the requirements to be visible. A total of 135000 systems are found. These are then queried in the WISE catalog to find their WISE magnitudes, 133660 of the systems are found in the WISE catalog. The WISE magnitudes are converted to flux density using (4), this is multiplied by the frequency of the WISE bands to give flux, and the slopes between the bands are found using (5).

The graph of WISE slopes vs disk brightness from Figure 16 is plotted again with the WISE data slopes for this new list of systems. There is a dense population of data points in the lower left quadrant, these systems have negative slope between W1 and W3 and mostly negative slope between W3 and W4. This indicates that a large amount of the systems in the list are stars without disks. The constraints used to produce the sample do not ensure that all the systems selected have protoplanetary disks. The most common types of stars are main sequence stars that have fully-formed planets and have dissipated their disk, which explains why this sample is dominated by these types of stars. The flux measured by WISE comes from the stellar photosphere; photospheres are typically at very high temperatures, therefore the energy they emit will be at very short wavelengths. The WISE detects some of this in the W1 and W2 bands but the slope between W1 and W3 is negative as there will be less flux detected at these wavelengths, as the star will emit its energy at much shorter wavelengths. Very little energy will be detected in the W3 and W4 bands as the star will emit little to no energy at these long wavelengths.

The rest of the graph is populated by different types of systems, many with circumstellar disks and possibly protoplanetary disks. The graph indicates which disks lie in the region of disks which may be bright, protoplanetary disks, that is, those with steep negative W1-W3

---

<sup>7</sup>Smaller magnitude means brighter star

<sup>8</sup>1 parsec (pc) = 3.26 light-years (31 trillion km)

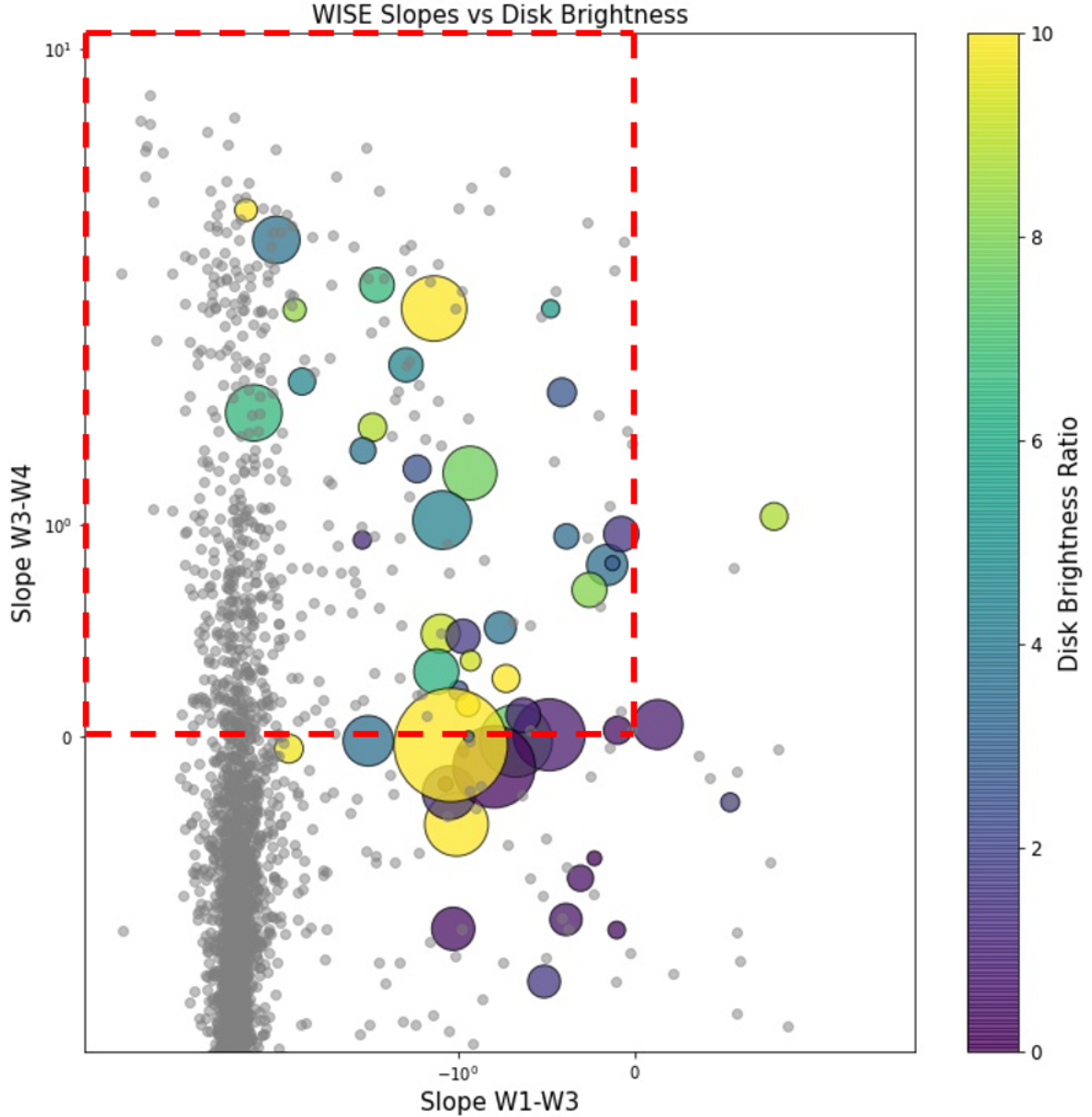


**Figure 17:** Plot of WISE Slopes vs Disk Brightness from Figure 17 with new data points plotted to show WISE slopes for disks which have yet to be imaged and have unknown disk brightness. The graph indicates which disks lie in the region of bright disks, that is, those with negative  $W1-W3$  slopes and positive  $W3-W4$  slopes. This is the region outlined in red. These disks are predicted to be bright and form a new sample of disks which should be imaged.

slopes and positive  $W3-W4$  slopes. 540 systems occupy this region, outlined in red. These disks are predicted to feature large cavities, as indicated by the slopes, and should be bright in scattered light images. This produces a sample of disks that can be proposed to be imaged by the VLT to obtain new images of disks with visible structure that can be used to learn more about planet formation.

## 11 Conclusions

Protoplanetary disks around young stars feature sub-structures that trace planets that are forming within the disk. Disks and their structures need to be studied in near-IR scattered light observations in order to further our understanding of planet formation. High-contrast images where the disk and structure is clearly visible is required for this. In order for the structure of the disk to be revealed in images, the entire disk must be illuminated by the stellar light. This is directly influenced by whether there is a large cavity present in the inner region of the disk. When the inner disk is depleted of material due to a large cavity, the light from the central star can reach the outer regions of the disk and light is scattered from each region in the disk, allowing the structure to be clear in images. Whereas, if there is a lot of disk material near the central star, this blocks the stellar light from reaching the rest of the disk which leads to the disk being shadowed and its structure cannot be clearly seen. This work looks to formulate a method for predicting the brightness of disks based on the change in flux emitted from a disk indicated by the WISE slopes for the disk.

The structure of protoplanetary disks can be inferred from Spectral Energy Distributions (SEDs). These graphs show the thermal emission from a disk as a function of wavelength of the emission. The SED for a star without a circumstellar disk is a blackbody curve. The circumstellar disk will emit energy at longer wavelengths to the star, as the material is colder, and these will appear as an increase in flux at longer wavelengths in the SED. The inner region of the disk will emit energy at short wavelengths, in the near-IR region, as the material is heated to high temperatures by the central star. Dust grains in the outer region of the disk are colder as they are further away from the stellar radiation and thus, will emit energy at longer wavelengths, in the far-IR region. The presence of a cavity in the inner region of a disk can be detected by SEDs as there will be a significant decrease in the flux detected in the near-IR region due to the depletion of material. There will be a subsequent increase in flux detected in the far-IR region, indicating there is a lot of material present in the outer region of the disk. By analysing the change in flux detected from disks, it can be predicted if there is a cavity present in the disk and therefore if the disk structure will be clearly seen in scattered light images.

The flux emitted by protoplanetary disks was measured by the WISE satellite. The WISE satellite performed an all-sky survey in the near-IR region centered at four wavelengths; 3.35, 4.6, 11.6, and 22.6  $\mu m$ . The flux measurements can be used to calculate the slopes of the flux across the four WISE bands. The slope between the WISE 1 and WISE 3 bands corresponds to the near-IR wavelengths and the inner region of the disks. The change in flux in the outer

region of the disk is shown by the slope between the WISE 3 and 4 bands. The presence of a cavity in a disk is indicated by a steep negative slope between the WISE 1 and WISE 3 bands, as this would demonstrate a significant decrease of flux detected from the inner disk due to the depletion of material. The disk is predicted to be bright in images if this is accompanied by a positive slope between WISE 3 and WISE 4, as this indicates there is material present in the outer region of the disk that will be illuminated by the stellar light.

The accuracy of this prediction can be determined by directly measuring the brightness ratio of disks that have been previously imaged. The brightness of a disk must be measured along its major axis due to the offset in the disk brightness caused by the disk inclination and scattering phase function of the disk. Light that is scattered from the near-side of the disk to us will be forward scattered, meaning there is more light scattered from this side. Therefore, this side of the disk will appear brighter compared to the back-side of the disk from which light is backward scattered. This causes an offset in the disk brightness along the minor axis of the disk. The brightness is measured along the major axis where the offset is least significant.

The amount of light scattered from different regions of the disk also depends on the distance from the center of the star. Further out in the disk, the light is spread over a larger area which causes affects the amount of light scattered. This is accounted for by considering the distance to the central star from each point where the brightness is measured. The amount of light scattered also depends on the brightness of the central star. To allow comparison between disks around different stellar spectral types, the dependence on the stellar flux must be cancelled. The brightness must also be average from the inner radius of the disk out to the outer radius to account for the disk extent and inclination.

Disk dust mass is an important factor that must also be considered as it directly affects the amount of light scattered by disks. Disks with a high dust mass can appear bright in images even if the flux detected from the disk does not indicate the presence of a large cavity. There is enough dust grains present in the disk to scatter sufficient light that the disk structure is largely visible in the image. Similarly, for disks where the geometry suggests it will be bright in scattered light, may appear faint if there is a low dust mass as there is not enough dust grains to scatter sufficient light in order for the structure to be visible.

The brightness ratios of the disks are compared to the WISE slopes and a trend can be seen. The brightest disks typically have steep negative slopes between WISE 1 and WISE 3 and positive slopes between WISE 3 and WISE 4. Exceptions to this trend are due to disks with very low dust mass, these disks will be faint in scattered light observations. Faint disks

have negative slopes between WISE 1 and WISE 3 but the slopes will be less steep or possibly positive in the case of shadowed disks where there is a lot of material in the inner region of the disk. They typically also have negative slopes between WISE 3 and WISE 4 which shows there is not much material in the outer disk and the structure will not be clear in images. Outliers to the trend for faint disks are due to disks with very high dust mass, these disks contain enough dust grains that will scatter a lot of light and allow the disk structure to be clear. Disks that are very inclined also appear much brighter in images as the majority of the light scattered from the disk is forward scattered which introduces a bias into the measurement.

The prediction for disks that will be bright in scattered light images is those with steep negative slopes between WISE 1 and WISE 3 bands, and positive slopes between WISE 3 and WISE 4 bands. However, it has been shown that this is not a characteristic that only bright protoplanetary disks display. Some faint disks show this trend but have a low dust mass that causes them to be faint in scattered light images. Inclined disks can also follow this trend, and while inclined disks are important to study for learning more about the structure and morphology of disks, their sub-structures are often not visible in images. Furthermore, protoplanetary disks are not the only types of systems that feature this trend in their WISE slopes.

This prediction was used to find a new sample of disks that should be bright in scattered light images and could be proposed as targets for future observations with the ESO’s VLT. A sample of 540 disks was found that are observable with the VLT and that are predicted to be bright based on their WISE slopes. However, only looking at the WISE slopes is not sufficient, other factors must be taken into consideration alongside this to form a more accurate, optimal sample of disks to be imaged. This sample can be refined further to filter out disks with low dust mass, disks that are not around young stars, and disks which have been previously imaged, as these will not be helpful in studying protoplanetary disk sub-structures in order to learn more about planet formation.

## 12 Future Work

This work has found a sample of 540 disks which are predicted to be bright based on their WISE slopes. There are many physical parameters that can be investigated to further refine the sample and determine the most optimal systems to image.

Many of the systems in the sample may have been previously imaged. We want to find a new sample of disks that have not been imaged in order to increase the amount of images that

can show us more about planet formation. The ESO's archive can be searched for the disks in the sample to filter out those that have scattered light images already obtained.

The stellar properties should be considered to classify the systems by age and luminosity. The age of the system is important to deduce if the system is a young star with a protoplanetary disk or if it is an older star with a circumstellar disk. The WISE slopes does not distinguish this so many of the disks in the plot that are predicted to be bright may be disks around older stars. These are known as AGB stars, intermediate or low-mass stars ( $1M_{\odot}$ ; $8M_{\odot}$ ) in their asymptotic giant branch phase, ?. Stars in this phase lose 80 percent of their mass to form enormous circumstellar disks. Post-AGB stars will feature a circumstellar disk, causing them to have SEDs and WISE slope measurements very similar to protoplanetary disks. The dispersal time for protoplanetary disks is approximately ten million years (Komaki et al. [2023]), for low mass stars, but decreases significantly for higher mass stars. It would be best to image as many systems from the sample that have ages below 10 Myr, to increase chances of observing disks with planets forming. The stellar ages can be estimated from spectrum of the sources which indicate stellar rotational periods. Stars rotate at different speeds depending on their age, younger stars will spin much faster than older stars. This can be measured from the Doppler shift of the star's spectral lines. The side of the star that is rotating away from us will be red-shifted and the side rotating towards us will be blue-shifted. The stronger the Doppler shift is, the broader the absorption lines become, the faster the star is rotating, and thus, the younger it is. The stellar spectra can indicate the stellar age in other ways, for example, from the strength of lithium spectral lines in a star's spectrum. The strength of lithium spectral lines decreases as stellar age increases, therefore, star's with stronger lithium lines in their spectra will be younger.

Once a sample of protoplanetary disks around young stars that have not been previously imaged is found, the disk dust mass can help determine which of these have the highest probability of being bright in scattered light. The disks which have the highest dust mass would be the most optimal to image as they will scatter more light due to the large amount of dust grains which will increase the chance of the disk structure being visible in the image. The dust mass can be determined from mm-observations with telescopes like ALMA (Atacama Large Millimetre Array). Dust grains scatter light at wavelengths similar to their size. Therefore, long wavelength observations will trace the large particles in the disk which make up the bulk of the disk mass. Disk mass estimates can be made based on mm continuum emission from the dust grains.

## 12.1 Plagiarism Declaration

I declare that this material, which I now submit for assessment, is my own work and that any assistance I received in its preparation is fully acknowledged and disclosed in the document. To the best of my knowledge and belief, all sources have been properly acknowledged, and the assessment task contains no plagiarism.

I understand that plagiarism, collusion, and/or copying are grave and serious offences and am aware that penalties could include a zero mark for this assessment, suspension, or expulsion from University of Galway. I have read the University of Galway code of practice regarding Academic Integrity (which covers plagiarism) at: [www.universityofgalway.ie/media/registrar/docs/QA220-Academic-Integrity-Policy-Final.pdf](http://www.universityofgalway.ie/media/registrar/docs/QA220-Academic-Integrity-Policy-Final.pdf)

I acknowledge that this assessment submission may be transferred and stored in a database for the purposes of data-matching to help detect plagiarism. I declare that this document was prepared by me for the purpose of partial fulfilment of requirements for the programme for which I am registered with the AUA. I also declare that this assignment, or any part of it, has not been previously submitted by me or any other person for assessment on this or any other course of study or another college.

NIAMH O TOOLE

Student Name

Niamh O Toole

17/11/2023

Student Signature

Date

## 12.2 Data References

This publication makes use of data products from the Wide-field Infrared Survey Explorer, which is a joint project of the University of California, Los Angeles, and the Jet Propulsion Laboratory/California Institute of Technology, funded by the National Aeronautics and Space Administration.

## References

R. D. Alexander and P. J. Armitage. Dust dynamics during protoplanetary disc clearing. , 375 (2):500–512, Feb. 2007. doi: 10.1111/j.1365-2966.2006.11341.x.

M. Benisty, C. Dominik, K. Follette, A. Garufi, C. Ginski, J. Hashimoto, M. Keppler, W. Kley, and J. Monnier. Optical and Near-infrared View of Planet-forming Disks and Protoplanets. In S. Inutsuka, Y. Aikawa, T. Muto, K. Tomida, and M. Tamura, editors, *Protostars and*

*Planets VII*, volume 534 of *Astronomical Society of the Pacific Conference Series*, page 605, July 2023. doi: 10.48550/arXiv.2203.09991.

J.-L. Beuzit, A. Vigan, D. Mouillet, K. Dohlen, R. Gratton, A. Boccaletti, J.-F. Sauvage, H. M. Schmid, M. Langlois, C. Petit, A. Baruffolo, M. Feldt, J. Milli, Z. Wahhaj, L. Abe, U. Anselmi, J. Antichi, R. Barette, J. Baudrand, P. Baudoz, A. Bazzon, P. Bernardi, P. Blanchard, R. Brast, P. Bruno, T. Buey, M. Carbillet, M. Carle, E. Cascone, F. Chapron, J. Charton, G. Chauvin, R. Claudi, A. Costille, V. D. Caprio, J. de Boer, A. Delboulb  , S. Desidera, C. Dominik, M. Downing, O. Dupuis, C. Fabron, D. Fantinel, G. Farisato, P. Feautrier, E. Fedrigo, T. Fusco, P. Gigan, C. Ginski, J. Girard, E. Giro, D. Gisler, L. Gluck, C. Gry, T. Henning, N. Hubin, E. Hugot, S. Incorvaia, M. Jaquet, M. Kasper, E. Lagadec, A.-M. Lagrange, H. L. Coroller, D. L. Mignant, B. L. Ruyet, G. Lessio, J.-L. Lizon, M. Llored, L. Lundin, F. Madec, Y. Magnard, M. Marteaud, P. Martinez, D. Mauzel, F. M  nard, D. Mesa, O. M  ller-Nilsson, T. Moulin, C. Moutou, A. Orign  , J. Parisot, A. Pavlov, D. Perret, J. Pragt, P. Puget, P. Rabou, J. Ramos, J.-M. Reess, F. Rigal, S. Rochat, R. Roelfsema, G. Rousset, A. Roux, M. Saisse, B. Salasnich, E. Santambrogio, S. Scuderi, D. Segransan, A. Sevin, R. Siebenmorgen, C. Soenke, E. Stadler, M. Suarez, D. Tiph  ne, M. Turatto, S. Udry, F. Vakili, L. B. F. M. Waters, L. Weber, F. Wildi, G. Zins, and A. Zurlo. SPHERE: the exoplanet imager for the very large telescope. *Astronomy & Astrophysics*, 631:A155, nov 2019. doi: 10.1051/0004-6361/201935251. URL <https://doi.org/10.1051%2F0004-6361%2F201935251>.

P. Bodenheimer, A. S. Grossman, W. M. Decampli, G. Marcy, and J. B. Pollack. Calculations of the evolution of the giant planets. , 41(2):293–308, Feb. 1980. doi: 10.1016/0019-1035(80)90012-3.

P. Bodenheimer, O. Hubickyj, and J. J. Lissauer. Models of the in situ formation of detected extrasolar giant planets,. *Icarus*, 143(1):2–14, 2000. ISSN 0019-1035. doi: <https://doi.org/10.1006/icar.1999.6246>. URL <https://www.sciencedirect.com/science/article/pii/S0019103599962462>.

A. P. Boss. Formation of Giant Gaseous Protoplanets by Gravitational Instability. In *Lunar and Planetary Science Conference*, Lunar and Planetary Science Conference, page 137, Mar. 1997.

W. Brandner. *Planet Formation: Theory, Observations, and Experiments*, volume 1 of *Cambridge Astrobiology*. Cambridge University Press, Cambridge, 1 edition, 2006. ISBN 9780521180740.

- P. Cassen, B. Smith, R. Miller, and R. Reynolds. Numerical experiments on the stability of preplanetary disks. *Icarus*, 48(3):377–392, 1981. ISSN 0019-1035. doi: [https://doi.org/10.1016/0019-1035\(81\)90052-X](https://doi.org/10.1016/0019-1035(81)90052-X). URL <https://www.sciencedirect.com/science/article/pii/001910358190052X>.
- E. I. Chiang and P. Goldreich. Spectral Energy Distributions of T Tauri Stars with Passive Circumstellar Disks. , 490(1):368–376, Nov. 1997. doi: 10.1086/304869.
- R. L. Doering, M. Meixner, S. T. Holfeltz, J. E. Krist, D. R. Ardila, I. Kamp, M. C. Clampin, and S. H. Lubow. Hd 97048’s circumstellar environment as revealed by a hubble space telescope acs coronagraphic study of disk candidate stars. *The Astronomical Journal*, 133(5):2122, mar 2007. doi: 10.1086/512610. URL <https://dx.doi.org/10.1086/512610>.
- R. Ellis. An Introduction to the Theory of Stellar Structure and Evolution, 2nd edn., by Dina Prialnik. *Contemporary Physics*, 52(5):490–490, Sept. 2011. doi: 10.1080/00107514.2011.580371.
- P. J. V. Garcia. *Physical Processes in Circumstellar Disks around Young Stars*. 2011.
- A. Garufi, G. Meeus, M. Benisty, S. P. Quanz, A. Banzatti, M. Kama, H. Canovas, C. Eiroa, H. M. Schmid, T. Stolker, A. Pohl, E. Rigliaco, F. Ménard, M. R. Meyer, R. van Boekel, and C. Dominik. Evolution of protoplanetary disks from their taxonomy in scattered light: Group I vs. Group II. , 603:A21, July 2017. doi: 10.1051/0004-6361/201630320.
- A. Garufi, M. Benisty, P. Pinilla, M. Tazzari, C. Dominik, C. Ginski, T. Henning, Q. Kral, M. Langlois, F. Ménard, T. Stolker, J. Szulagyi, M. Villenave, and G. van der Plas. Evolution of protoplanetary disks from their taxonomy in scattered light: spirals, rings, cavities, and shadows. , 620:A94, Dec. 2018. doi: 10.1051/0004-6361/201833872.
- A. Garufi, C. Dominik, C. Ginski, M. Benisty, R. G. van Holstein, T. Henning, N. Pawellek, C. Pinte, H. Avenhaus, S. Facchini, R. Galicher, R. Gratton, F. Ménard, G. Muro-Arena, J. Milli, T. Stolker, A. Vigan, M. Villenave, T. Moulin, A. Origone, F. Rigal, J. F. Sauvage, and L. Weber. A SPHERE survey of self-shadowed planet-forming disks. , 658:A137, Feb. 2022. doi: 10.1051/0004-6361/202141692.
- A. Garufi, C. Ginski, R. G. van Holstein, M. Benisty, C. F. Manara, S. Pérez, P. Pinilla, Á. Ribas, P. Weber, J. Williams, L. Cieza, C. Dominik, S. Facchini, J. Huang, A. Zurlo, J. Bae, J. Hagelberg, T. Henning, M. R. Hogerheijde, M. Janson, F. Ménard, S. Messina, M. R. Meyer, C. Pinte, S. P. Quanz, E. Rigliaco, V. Roccagliata, H. M. Schmid, J. Szulágyi,

R. van Boekel, Z. Wahhaj, J. Antichi, A. Baruffolo, and T. Moulin. The SPHERE view of the Taurus star-forming region. *arXiv e-prints*, art. arXiv:2403.02158, Mar. 2024. doi: 10.48550/arXiv.2403.02158.

C. Ginski, T. Stolker, P. Pinilla, C. Dominik, A. Boccaletti, J. de Boer, M. Benisty, B. Biller, M. Feldt, A. Garufi, C. U. Keller, M. Kenworthy, A. L. Maire, F. Ménard, D. Mesa, J. Milli, M. Min, C. Pinte, S. P. Quanz, R. van Boekel, M. Bonnefoy, G. Chauvin, S. Desidera, R. Gratton, J. H. V. Girard, M. Keppler, T. Kopytova, A.-M. Lagrange, M. Langlois, D. Rouan, and A. Vigan. Direct detection of scattered light gaps in the transitional disk around HD 97048 with VLT/SPHERE. *Astronomy & Astrophysics*, 595:A112, nov 2016. doi: 10.1051/0004-6361/201629265. URL <https://doi.org/10.1051%2F0004-6361%2F201629265>.

P. Goldreich and S. Tremaine. The excitation of density waves at the Lindblad and corotation resonances by an external potential. , 233:857–871, Nov. 1979. doi: 10.1086/157448.

A. Komaki, S. Fukuhara, T. K. Suzuki, and N. Yoshida. Simulations of protoplanetary disk dispersal: Stellar mass dependence of the disk lifetime, 2023.

M. R. Krumholz, E. Telles, R. Dupke, and D. Lazzaro. Star formation in molecular clouds. In *AIP Conference Proceedings*. AIP, 2011. doi: 10.1063/1.3636038. URL <https://doi.org/10.1063%2F1.3636038>.

G. Laughlin and P. Bodenheimer. Nonaxisymmetric Evolution in Protostellar Disks. , 436:335, Nov. 1994. doi: 10.1086/174909.

J. Mariotti and D. Alloin. *Planets outside the solar system : theory and observations*. NATO science series. Series C, Mathematical and physical sciences ; v. 532. Kluwer Academic Publishers, Dordrecht ; London, 1999. ISBN 0792357086.

G. D. Mulders, M. Min, C. Dominik, J. H. Debes, and G. Schneider. Why circumstellar disks are so faint in scattered light: the case of HD 100546. , 549:A112, Jan. 2013. doi: 10.1051/0004-6361/201219522.

R. Mundt and T. P. Ray. Optical outflows from Herbig Ae/Be stars and other high luminosity young stellar objects. In P. S. The, M. R. Perez, and E. P. J. van den Heuvel, editors, *The Nature and Evolutionary Status of Herbig Ae/Be Stars*, volume 62 of *Astronomical Society of the Pacific Conference Series*, page 237, Jan. 1994.

G. Neugebauer, H. J. Habing, R. van Duinen, H. H. Aumann, B. Baud, C. A. Beichman, D. A. Beintema, N. Boggess, P. E. Clegg, T. de Jong, J. P. Emerson, T. N. Gautier, F. C. Gillett,

- S. Harris, M. G. Hauser, J. R. Houck, R. E. Jennings, F. J. Low, P. L. Marsden, G. Miley, F. M. Olnon, S. R. Pottasch, E. Raimond, M. Rowan-Robinson, B. T. Soifer, R. G. Walker, P. R. Wesselius, and E. Young. The Infrared Astronomical Satellite (IRAS) mission. , 278: L1–L6, Mar. 1984. doi: 10.1086/184209.
- P. Pinilla, M. Tazzari, I. Pascucci, A. N. Youdin, A. Garufi, C. F. Manara, L. Testi, G. van der Plas, S. A. Barenfeld, H. Canovas, E. G. Cox, N. P. Helder, L. M. Pérez, and N. van der Marel. Homogeneous analysis of the dust morphology of transition disks observed with alma: Investigating dust trapping and the origin of the cavities. *The Astrophysical Journal*, 859(1):32, May 2018. ISSN 1538-4357. doi: 10.3847/1538-4357/aabf94. URL <http://dx.doi.org/10.3847/1538-4357/aabf94>.
- T. Poppe, J. Blum, and T. Henning. Analogous Experiments on the Stickiness of Micron-sized Preplanetary Dust. , 533(1):454–471, Apr. 2000. doi: 10.1086/308626.
- R. G. Prinn. Chemistry and Evolution of Gaseous Circumstellar Disks. In E. H. Levy and J. I. Lunine, editors, *Protostars and Planets III*, page 1005, Jan. 1993.
- T. Stolker, C. Dominik, H. Avenhaus, M. Min, J. de Boer, C. Ginski, H. M. Schmid, A. Juhasz, A. Bazzon, L. B. F. M. Waters, A. Garufi, J. C. Augereau, M. Benisty, A. Boccaletti, T. Henning, M. Langlois, A. L. Maire, F. Ménard, M. R. Meyer, C. Pinte, S. P. Quanz, C. Thalmann, J. L. Beuzit, M. Carillet, A. Costille, K. Dohlen, M. Feldt, D. Gisler, D. Mouillet, A. Pavlov, D. Perret, C. Petit, J. Pragt, S. Rochat, R. Roelfsema, B. Salasnich, C. Soenke, and F. Wildi. Shadows cast on the transition disk of HD 135344B. Multiwavelength VLT/SPHERE polarimetric differential imaging. , 595:A113, Nov. 2016. doi: 10.1051/0004-6361/201528039.
- I. Tilling, P. Woitke, G. Meeus, A. Mora, B. Montesinos, P. Riviere-Marichalar, C. Eiroa, W. F. Thi, A. Isella, A. Roberge, C. Martin-Zaidi, I. Kamp, C. Pinte, G. Sandell, W. D. Vacca, F. Ménard, I. Mendigutía, G. Duchêne, W. R. F. Dent, G. Aresu, R. Meijerink, and M. Spaans. Gas modelling in the disc of HD 163296. , 538:A20, Feb. 2012. doi: 10.1051/0004-6361/201116919.
- G. van der Plas, C. M. Wright, F. Ménard, S. Casassus, H. Canovas, C. Pinte, S. T. Maddison, K. Maaskant, H. Avenhaus, L. Cieza, S. Perez, and C. Ubach. Cavity and other radial substructures in the disk around HD 97048. *Astronomy & Astrophysics*, 597:A32, dec 2016. doi: 10.1051/0004-6361/201629523. URL <https://doi.org/10.1051%2F0004-6361%2F201629523>.

S. J. Weidenschilling and J. N. Cuzzi. Formation of Planetesimals in the Solar Nebula. In E. H. Levy and J. I. Lunine, editors, *Protostars and Planets III*, page 1031, Jan. 1993.

J. P. Williams and L. A. Cieza. Protoplanetary disks and their evolution. *Annual Review of Astronomy and Astrophysics*, 49(1):67–117, Sept. 2011. ISSN 1545-4282. doi: 10.1146/annurev-astro-081710-102548. URL <http://dx.doi.org/10.1146/annurev-astro-081710-102548>.

P. Woitke. Modelling and interpretation of SEDs. In *European Physical Journal Web of Conferences*, volume 102 of *European Physical Journal Web of Conferences*, page 00007, Sept. 2015. doi: 10.1051/epjconf/201510200007.

E. L. Wright, P. R. M. Eisenhardt, A. K. Mainzer, M. E. Ressler, R. M. Cutri, T. Jarrett, J. D. Kirkpatrick, D. Padgett, R. S. McMillan, M. Skrutskie, S. A. Stanford, M. Cohen, R. G. Walker, J. C. Mather, D. Leisawitz, I. Gautier, Thomas N., I. McLean, D. Benford, C. J. Lonsdale, A. Blain, B. Mendez, W. R. Irace, V. Duval, F. Liu, D. Royer, I. Heinrichsen, J. Howard, M. Shannon, M. Kendall, A. L. Walsh, M. Larsen, J. G. Cardon, S. Schick, M. Schwalm, M. Abid, B. Fabinsky, L. Naes, and C.-W. Tsai. The Wide-field Infrared Survey Explorer (WISE): Mission Description and Initial On-orbit Performance. , 140(6):1868–1881, Dec. 2010. doi: 10.1088/0004-6256/140/6/1868.

## 13 Appendices

### 13.1 Appendix A. Python Code Written in this Work

### 13.2 Necessary Libraries

```
1 import numpy as np
2 import matplotlib.pyplot as plt
3 import pandas as pd
4 import astropy
5 from astroquery.vizier import Vizier
6 import astropy.units as u
7 import astropy.coordinates as coord
8 from astropy.coordinates import SkyCoord
9 from astropy.coordinates import Angle
10 from astropy.table import Table
```

```

11  from astropy.io import fits
12  from astropy.utils.data import get_pkg_data_filename
13  from astropy.wcs import WCS
14  from photutils.aperture import CircularAperture
15  from photutils.aperture import aperture_photometry
16  from photutils.aperture import ApertureStats
17  from matplotlib.colors import SymLogNorm

```

*Listing 1: Necessary python libraries for this work*

### 13.3 Query Disk Sample WISE Magnitudes

```

1  # Read in a file with the list of system names
2  with open('starlist.txt') as starlist:
3      lines = starlist.read().splitlines()
4
5  # Define a list to hold all the system names
6  stars = []
7  # Append the list to hold the names from the file
8  for line in lines:
9      stars.append(line)
10
11 # Define a function that takes each system name from the list and
12 # queries the WISE catalog in Vizier for the magnitude values for the
13 # star
14
15 def wise_mag(stars):
16     for star_name in stars:
17         # query WISE catalog for the star
18         v = Vizier(columns=['*', '_r'], catalog='II/311/wise')
19
20         # query a small region of 2 arcsec around the star to ensure
21         # only data for this star is returned
22         star_result = v.query_region(star_name, radius='2s')
23
24         # return the wise data table for the star
25         wise_table = star_result['II/311/wise']
26
27         # convert the astropy table to a pandas data frame
28         df = wise_table.to_pandas()

```

```

25
26     # extract the wise magnitudes from the table
27
28     magnitudes = df[['W1mag', 'W2mag', 'W3mag', 'W4mag']].iloc[0].
29     tolist()
30
31
32     #print the magnitudes
33     print(magnitudes)
34
35
36     # Run the function for the list of systems defined above
37     wise_mag(stars)

```

*Listing 2: Query each star from the sample in Vizier for its WISE magnitudes*

### 13.4 Calculate the WISE Slopes using the WISE Magnitudes

```

1  from contextlib import redirect_stdout
2
3  # Write the WISE magnitude values to a file
4  with open('magnitudes.txt', 'w') as f:
5      with redirect_stdout(f):
6          wise_mag(stars)
7
8  # Read in the file and define lists to hold the WISE 1, 2, 3, and 4
9  # magnitude values for each system
10 with open("magnitudes.txt") as data:
11     lines = data.read().splitlines()
12
13     # WISE 1 magnitudes
14     W1 = []
15     for line in lines:
16         Columns = line.split(',')
17         W1.append(Columns[0])
18
19     # WISE 2 magnitudes
20     W2 = []
21     for line in lines:
22         Columns = line.split(',')
23         W2.append(Columns[1])

```

```

24 # WISE 3 magnitudes
25 W3 = []
26 for line in lines:
27     Columns = line.split(',')
28     W3.append(Columns[2])
29
30 # WISE 4 magnitudes
31 W4 = []
32 for line in lines:
33     Columns = line.split(',')
34     W4.append(Columns[3])
35
36 # Convert the elements in the lists to floats
37 W1_mag = [float(a) for a in W1]
38 W2_mag = [float(b) for b in W1]
39 W3_mag = [float(c) for c in W1]
40 W4_mag = [float(d) for d in W1]
41
42 # Define an array for the magnitudes for each WISE band
43 W1_magnitudes = np.array(W1_mag)
44 W2_magnitudes = np.array(W2_mag)
45 W3_magnitudes = np.array(W3_mag)
46 W4_magnitudes = np.array(W4_mag)
47
48 # Convert the magnitudes to fluxes using the formula and correct
49 # conversion factor for each band.
50 W1_flux = np.log(309.540 * 10**(-W1_magnitudes/2.5))
51 W2_flux = np.log(171.787 * 10**(-W2_magnitudes/2.5))
52 W3_flux = np.log(31.674 * 10**(-W3_magnitudes/2.5))
53 W4_flux = np.log(8.363 * 10**(-W4_magnitudes/2.5))
54
55 # Define the wavelength values for each of the WISE bands
56 W1_wavelength = np.log(3.35)
57 W2_wavelength = np.log(4.6)
58 W3_wavelength = np.log(11.6)
59 W4_wavelength = np.log(22.1)
60
61 # Calculate the slopes between the W1 and W3 bands and between the
62 # W3 and W4 bands

```

```

61     slope_W1W3 = (W3_flux - W1_flux) / (W3_wavelength - W1_wavelength)
62     slope_W3W4 = (W4_flux - W3_flux) / (W4_wavelength - W3_wavelength)

```

### 13.5 Measuring the Brightness Ratio of the Disks in the Sample from the High-Contrast Images

```

1  # Function 1: Load image from FITS file into a numpy array
2  def load_image(file_path):
3      fits_image = get_pkg_data_filename(file_path)
4      image_data = fits.getdata(fits_image, ext=0)
5      image = image_data[1]
6      return image
7
8  # Function 2: Generate aperture coordinates along the major axis
9  def generate_aperture_coordinates(image, angle_major_axis,
10     num_apertures, lower_left=True):
11      # Get the center of the image
12      center_y, center_x = np.array(image) / 2.0
13
14      # Convert the angle to radians
15      angle_rad = np.radians(angle_major_axis)
16
17      # Generate equally spaced distances along the major axis
18      distances = np.linspace(-1, 1, num_apertures) # Values between
19      -1 and 1 for normalized distances
20      distances *= np.max(image) / 2.0 # Scale distances based on
21      image size
22
23      # Calculate coordinates along the specified axis
24      x_coordinates = center_x + distances * np.cos(angle_rad)
25      y_coordinates = center_y + distances * np.sin(angle_rad)
26
27      return x_coordinates, y_coordinates
28
29  # Function 3: Perform aperture photometry at a single position
30  def perform_aperture_photometry(image, x, y, aperture_radius):
31      # Define the position for the aperture
32      positions = [(x, y)]

```

```

30
31     # Create a circular aperture centered at the specified position
32     # with the given radius
33
34     apertures = CircularAperture(positions, r=aperture_radius)
35
36
37
38     return flux_mean
39
40
41     # Function 4: Visualize the image with apertures
42
43     def visualize_image_with_apertures(image, x_coordinates,
44                                         y_coordinates, large_aperture_x, large_aperture_y,
45                                         large_aperture_radius):
46
47         plt.figure(figsize=(10,10))
48
49         plt.imshow(image, cmap='gray', norm=SymLogNorm(linthresh=0.001,
50                                                       vmin=-10e-3, vmax=10e-3))
51
52         plt.scatter(x_coordinates, y_coordinates, color='red', marker='x',
53                     label='Aperture Centres')
54
55
56         # Plot large aperture in the lower-left region for measuring the
57         # background noise
58
59         large_aperture = CircularAperture([(large_aperture_x,
60                                             large_aperture_y)], r=large_aperture_radius)
61
62         large_aperture.plot(plt.gca(), color='blue', alpha=0.5, label='
63                             Large Aperture')
64
65
66         plt.tight_layout()
67
68         plt.savefig('image.jpg')
69
70         plt.legend(loc='center left', bbox_to_anchor=(1, 0.5))
71
72         plt.xticks(fontsize=14)
73
74         plt.yticks(fontsize=14)
75
76         plt.show()
77
78
79     # Function 5: Plot the flux of the disk relative to the distance
80     # from the centre
81
82     def plot_brightness_profile(image, angle_major_axis, num_apertures,
83                                aperture_radius, noise):

```

```

59         center_y, center_x = np.array(image.shape) / 2.0
60
61         x_coordinates, y_coordinates = generate_aperture_coordinates(
62             image.shape, angle_major_axis, num_apertures)
63
64         # Calculate distances from the center for each aperture whose
65         # fluxes do not exceed the background noise
66         distances_from_center = []
67         relative_brightness = []
68         for x, y in zip(x_coordinates, y_coordinates):
69             aperture_flux = perform_aperture_photometry(image, x, y,
70                 aperture_radius)
71
72             # If the flux in an aperture is less than the noise, skip
73             # that aperture
74             if aperture_flux < noise:
75                 continue
76
77             # Calculate the distance in pixels of each aperture from the
78             # center of the image
79             distance_pixel = np.sqrt((x - center_x)**2 + (y - center_y)
80             **2)
81
82             # Convert the distance to arcseconds using the pixel scale
83             constant
84             dist_arcsec = distance_pixel * 0.012251
85             distances_from_center.append(dist_arcsec)
86
87             # Multiply aperture flux by distance and append to the
88             # brightness profile list
89             rel_flux = aperture_flux * (4 * np.pi * dist_arcsec**2)
90             relative_brightness.append(rel_flux)
91
92             # Convert lists to arrays for plotting
93             distances = np.array(distances_from_center)
94             rel_brightness = np.array(relative_brightness)
95             # Calculate the average of the surface brightness
96             brightness = np.average(rel_brightness)
97
98             # Plot brightness profile relative to distances
99             plt.plot(distances, rel_brightness, marker='o', linestyle='--')
100            plt.xlabel('Distance from Center (arcsec)')

```



```

127     if band == "Jmag":
128         f_jy = f0_J * 10**(-0.4*mag_2mass)
129     if band == "Hmag":
130         f_jy = f0_H * 10**(-0.4*mag_2mass)
131     if band == "Kmag":
132         f_jy = f0_K * 10**(-0.4*mag_2mass)
133
134     return f_jy
135
136
137 # Master function: Wrapper for functions 1-6
138 def measure_radial_brightness_profile(star_name, file_path,
139                                         angle_major_axis, num_apertures, aperture_radius):
140
141     # Function 1: Load image
142
143     image = load_image(file_path)
144
145
146     # Function 2: Generate aperture coordinates along the major axis
147
148     x_coordinates, y_coordinates = generate_aperture_coordinates(
149         image.shape, angle_major_axis, num_apertures)
150
151
152     # Find coordinates of a point in the lower-left region
153
154     lower_left_x, lower_left_y = 200, 200
155
156
157     # Define a large aperture in the lower-left region
158
159     large_aperture_radius = 100
160
161     aper = CircularAperture((lower_left_x, lower_left_y),
162                             large_aperture_radius)
163
164
165     # Calculate the noise within the large aperture
166
167     aperstats = ApertureStats(image, aper)
168
169     noise = aperstats.std
170
171
172     # Visualize the image with apertures, including the large
173     # aperture
174
175     visualize_image_with_apertures(image, x_coordinates,
176                                     y_coordinates, lower_left_x, lower_left_y, large_aperture_radius)
177
178
179     # Function 3: Perform aperture photometry and store results
180     # along the major axis
181
182     brightness_profile = []
183
184     aperture_values = []

```

```

160         for x, y in zip(x_coordinates, y_coordinates):
161             flux = perform_aperture_photometry(image, x, y,
162                                                 aperture_radius)
163
164             # Check if flux equals the noise in the image
165             if flux < noise:
166                 continue
167             brightness_profile.append(flux)
168             aperture_values.append(y)
169
170             # Plot radial brightness profile
171             plt.plot(brightness_profile, marker='o', linestyle='--', label='
172 Radial Brightness Profile')
173             plt.xlabel('Aperture Index')
174             plt.ylabel('Flux')
175             plt.title('Radial Brightness Profile along Major Axis')
176             plt.legend()
177             plt.show()
178
179             # Plot radial brightness profile
180             plt.plot(aperture_values, brightness_profile, marker='o',
181                      linestyle='--', label='Radial Brightness Profile')
182             plt.xlabel('Aperture Index')
183             plt.ylabel('Flux (Jy)')
184             plt.title('Radial Brightness Profile along Major Axis')
185             plt.legend()
186             plt.tight_layout()
187             plt.savefig('brightness_profile_hd97048.jpg')
188             plt.show()
189
190             # Plot brightness profile relative to distances
191             #plot_brightness_profile(image, angle_major_axis, num_apertures,
192             #aperture_radius, noise)
193
194             # Brightness of disk
195             disk_brightness = plot_brightness_profile(image,
196                                         angle_major_axis, num_apertures, aperture_radius, noise)
197
198             # Find the flux of the star

```

```

194     star_flux = star_mag(star_name, file_path)
195
196     # Calculate the flux of the disk relative to the flux of the
197     # star
198     rel_flux = disk_brightness / star_flux
199     print(rel_flux)
200
201
202     return brightness_profile
203
204
205     # Example usage:
206
207     star_name = 'hd97048'
208     file_path = 'HD__97048_SPHERE_2019-05-24_K.fits'
209     angle_major_axis = 90 # angle of the major axis
210     num_apertures = 500 # number of apertures to plot
211     aperture_radius = 4 # aperture radius for photometry
212
213
214     # Run the function
215     brightness_profile = measure_radial_brightness_profile(star_name,
216     file_path, angle_major_axis, num_apertures, aperture_radius)

```

*Listing 3: Measure the brightness ratio of the disks in the sample from their high contrast images*

## 13.6 Plotting the WISE Slopes against the Disk Brightness Ratios

```

1 # Open the data file and read in all the lines
2 filename = 'data.txt'
3 with open(filename) as data:
4     lines = data.read().splitlines()
5
6     # Define lists to hold the disk brightness ratios and slopes and
6     # append with the values from the correct columns
7     brightness_ratio = []
8     for line in lines:
9         Columns = line.split(',')
10        scaled_brightness.append(Columns[0])
11
12     slope_W1W3 = []
13     for line in lines:
14         Columns = line.split(',')

```

```

15     slope_W1W3.append(Columns[1])
16
17 slope_W3W4 = []
18 for line in lines:
19     Columns = line.split(' ')
20     slope_W3W4.append(Columns[2])
21
22 # Open the data file with the dust mass values and read in all the
23 # lines
24 file = 'dust mass.txt'
25 with open(file) as values:
26     read = values.read().splitlines()
27
28 # Define a list to hold the dust mass values
29 dust_mass = []
30 for line in read:
31     Columns = line.split(' ')
32     dust_mass.append(Columns[1])
33
34 # Convert to floats
35 brightness_ratio = [float(a) for a in brightness_ratio]
36 slope_W1W3 = [float(b) for b in slope_W1W3]
37 slope_W3W4 = [float(c) for c in slope_W3W4]
38 dust_mass = [float(d) for d in dust_mass]
39
40 # Set the size scale using the dust mass values
41 s = [500*n for n in dust_mass]
42
43 # Plot the data
44 plt.figure(figsize=(10, 10))
45 plt.scatter(slope_W1W3, slope_W3W4, c=scaled_brightness, cmap='viridis', s=s, edgecolors='k', alpha=0.75)
46 cbar = plt.colorbar()
47 cbar.ax.tick_params(labelsize=12)
48 cbar.set_label(label='Disk Brightness Ratio', fontsize=15)
49 plt.xlabel('Slope W1-W3', fontsize=15)
50 plt.ylabel('Slope W3-W4', fontsize=15)
51 plt.title('WISE Slopes vs Disk Brightness', fontsize=15)
52 plt.xticks(ticks=slope_W1W3, labels=slope_W1W3, fontsize=12)

```

```

52 plt.yticks(ticks=slope_W3W4, labels=slope_W3W4, fontsize=12)
53 plt.xscale('symlog')
54 plt.yscale('symlog')
55 plt.ylim(0, 10)
56 plt.minorticks_on()
57 # Annotate zero point
58 plt.text(0, -0.5, '0')
59 plt.tight_layout()
60 plt.savefig('plot.jpg')
61 plt.show()

```

*Listing 4:* Plot the WISE slopes for each disk on a graph and use a colourbar to indicate the brightness ratio and a size scale to indicate the disk dust mass relative to the stellar mass

### 13.7 Finding a New Sample of Disks that are Predicted to be Bright

```

1 # Query Gaia catalog to find systems observable with the VLT
2 gaia_result = Vizier(catalog='I/345/gaia2', columns=['*', '_RAJ2000',
3 , '_DEJ2000'], row_limit=1000000, timeout=120).query_constraints(
4 DE_ICRS='<30', Gmag='<13.5', Plx='2.0..5.0')[0]
5
6 # Query the WISE catalogue for this sample
7 wise_result = Vizier(catalog='II/311/wise', row_limit=200000,
8 timeout=120).query_region(gaia_result, radius="2s")[0]
9
10 # Convert result to pandas dataframe
11 data = wise_result.to_pandas()
12
13 # Convert required columns to arrays
14 stars = data['WISE'].to_numpy()
15 RA_DEC = data[['RAJ2000', 'DEJ2000']].to_numpy()
16 W1mag = data['W1mag'].to_numpy()
17 W2mag = data['W2mag'].to_numpy()
18 W3mag = data['W3mag'].to_numpy()
19 W4mag = data['W4mag'].to_numpy()
20
21 # Calculate the WISE slopes using the same formula from earlier
22 # Convert the magnitudes to flux density
23 W1_flux_density = (309.540 * 10**(-W1mag/2.5))

```

```

21 W2_flux_density = (171.787 * 10**(-W2mag/2.5))
22 W3_flux_density = (31.676 * 10**(-W3mag/2.5))
23 W4_flux_density = (8.363 * 10**(-W4mag/2.5))
24
25 # Frequency of each of the WISE bands
26 W1_freq = 8.95e-13
27 W2_freq = 6.52e-13
28 W3_freq = 2.59e-13
29 W4_freq = 1.36e-13
30
31 #Convert flux density to flux
32 W1_flux = np.log10(W1_freq * W1_flux_d)
33 W2_flux = np.log10(W2_freq * W2_flux_d)
34 W3_flux = np.log10(W3_freq * W3_flux_d)
35 W4_flux = np.log10(W4_freq * W4_flux_d)
36
37 # wavelength values for each WISE band
38 W1_wavelength = np.log10(3.35)
39 W2_wavelength = np.log10(4.6)
40 W3_wavelength = np.log10(11.6)
41 W4_wavelength = np.log10(22.1)
42
43 # Calculate the slopes
44 slope1 = (W3_flux - W1_flux) / (W3_wavelength - W1_wavelength)
45 slope2 = (W4_flux - W3_flux) / (W4_wavelength - W3_wavelength)
46
47 # Plot the WISE slopes for the new sample on the graph from before
48 plt.figure(figsize=(10, 10))
49 plt.scatter(slope_W1W3, slope_W3W4, c=scaled_brightness, cmap='viridis', s=s, edgecolors='k', alpha=0.75)
50 cbar = plt.colorbar()
51 cbar.ax.tick_params(labelsize=12)
52 cbar.set_label(label='Disk Brightness Ratio', fontsize=15)
53 plt.clim(0, 10)
54 plt.scatter(slope1, slope2, c='gray', alpha=0.5)
55 plt.xlabel('Slope W1-W3', fontsize=15)
56 plt.ylabel('Slope W3-W4', fontsize=15)
57 plt.title('WISE Slopes vs Disk Brightness', fontsize=15)
58 plt.xscale('symlog')

```

```

59 plt.yscale('symlog')
60 plt.ylim(-1.5)
61 plt.minorticks_on()
62 plt.tight_layout()
63 plt.savefig('new_sample.jpg')
64 plt.show()
65
66 # Extract the RA and DEC coordinates for the new sample
67 sample_stars_coords = []
68 for i in range(len(RA_DEC)):
69     if slope1[i] < 0 and slope2[i] > 0:
70         sample_stars_coords.append(RA_DEC[i])

```

*Listing 5: Find the sample of disks that are observable with the VLT*

## 13.8 New Sample of Disks Predicted to be Bright

**Table 4:** Sources, WISE slopes and disk contrast values.

Source	Right Ascension ( $^{\circ}$ , '')	Declination ( $^{\circ}$ , '')
HD49662	06 48 57.73663	-15 08 41.0004
V* VV Ori	05 33 31.4464933704	-01 09 21.859452468
HD37303	05 37 27.3575332104	-05 56 18.204499212
HD36408A	05 32 14.1413460264	+17 03 29.278298880
HD200266	21 08 47.6073020832	-76 12 44.890135056
HD68478	08 10 20.5684356576	-49 14 14.494042104
HD93695	10 47 44.3174678544	-59 52 30.921185136
HD37150	05 36 15.0278258688	-05 38 52.514534220
HD39777	05 54 34.6960877928	-04 03 52.967826720
* sig Ori E	05 38 47.2050040320	-02 35 40.521424812
HD162220	17 51 12.5549492856	-30 33 24.729052680
* sig Ori D	05 38 45.6253355112	-02 35 58.894678824
V* V901 Ori	05 40 56.3704617744	-01 30 25.856677224
HD175427	18 54 32.85472	+20 36 55.0835
HD142348	15 56 43.9892448816	-53 47 20.413706640
HD41253	06 03 58.1423807568	+02 51 51.717987360
HD77366	09 00 42.0646463160	-38 25 10.134802560
HD36958	05 35 04.7875827888	-04 43 54.626071800
HD37058	05 35 33.3539646576	-04 50 15.181113696
HD72019	08 28 15.7597816152	-51 46 13.391309388
HD160147	17 40 09.7252429560	-39 12 17.931675168
HD37641	05 39 56.5689787560	-01 55 36.192131112
HD144696	16 09 38.6698701312	-52 06 55.071321948
HD37699	05 40 20.1907288344	-02 26 08.229954660
HD36629	05 32 57.0824474232	-04 33 59.339585016
HD37674	05 40 13.5394904328	-01 27 45.249257592
HD163304	17 57 17.3044105946	-38 46 57.608679994
HD36981	05 35 06.1984793208	-05 12 15.917207580
HD76060	08 52 02.4492347352	-46 17 19.845385800
HD162655	17 53 16.7666347296	-27 37 44.267804760
HD294271	05 38 36.5498973360	-02 33 12.757741200
HD68496	08 10 27.2436784248	-49 09 50.928876288
HD36310	05 30 57.7461396576	+04 40 07.430781972
HD85810	09 52 39.7600494360	-55 27 14.008970124
HD166107	18 10 06.8381721480	-23 46 22.605346452
HD175037	18 53 27.9358180128	+00 52 13.041919884
V* V1454 Aql	19 26 05.1331956240	+03 31 09.730192512
V* V1665 Aql	18 56 09.9028820904	+07 56 08.222019612
HD144901	16 10 36.1410114360	-51 58 07.566192876
HD161703	17 48 12.2546659680	-28 45 46.484827668
HD165918	18 09 04.6455519240	-19 52 30.817060860
HD150167	16 41 23.9343010344	-46 23 08.559928644
HD56856	07 17 05.4107889816	-37 06 48.742269480
HD36842	05 34 26.2625938087	-04 22 16.370962498
HD182275	19 23 21.0789380904	+14 42 46.880521632
HD88068	10 07 31.0035824520	-57 32 59.848838340
HD34835	05 20 07.7749297632	-05 50 46.009713984
HD164147	18 00 50.9573127960	-24 47 18.667272588
HD38087	05 43 00.5754723576	-02 18 45.389406240
HD318101	17 40 02.2638142656	-32 09 36.927973584

**Table 5:** Sources, WISE slopes and disk contrast values.

Source	Right Ascension ( $^{\circ}$ ' '')	Declination ( $^{\circ}$ ' '')
HD152540	16 55 53.4917721408	-43 04 15.104313840
V* V1099 Ori	05 32 13.0812769464	-01 36 01.745707500
HD95307	10 59 06.1392865032	-61 07 40.087912008
HD231160	19 19 52.0586090040	+14 03 50.336350308
HD37373	05 37 50.8348147704	-06 43 19.520133996
HD164226	18 01 10.3252996896	-23 33 15.658373808
HD152940	16 58 17.9862708096	-41 04 35.055798240
HD37389	05 38 08.0088995496	-01 45 07.824199572
HD37370	05 38 06.5148992564	-00 11 03.466277676
HD87042	10 00 28.8188978832	-59 59 32.568274464
HD37927	05 41 52.8456399024	-02 47 54.883944492
HD150806	16 45 22.1720166696	-44 45 50.053760928
HD96492	11 06 07.7246159712	-61 03 16.046418708
HD82003	09 27 21.2085178320	-53 58 07.880468592
HD173437	18 45 26.7687839736	-03 13 53.580136656
HD164739	18 03 37.9735593312	-23 08 17.418853644
HD36999	05 35 14.0074226880	-05 49 36.276923784
HD93191	10 44 27.5554190760	-59 53 05.535548556
HD93114	10 43 48.3981271008	-59 06 05.500602792
HD195310	20 29 49.4433953400	+20 36 18.430317072
HD166289	18 10 42.0851685456	-17 55 05.309277960
HD176709	19 01 29.2321741296	+04 15 28.576651572
HD74580	08 42 53.0614868352	-48 07 41.163227544
HD160167	17 39 53.5182631800	-32 22 32.207373048
HD145448A	16 13 30.1708494528	-51 37 02.755191396
HD176217	18 59 07.6043386008	+03 25 40.255743108
HD123026	14 07 13.1617841856	-61 25 24.642512004
HD148988	16 34 06.9962527560	-48 04 46.939482480
HD175427	18 54 32.85472	+20 36 55.0835
HD180826	19 18 43.0706107104	-17 00 30.703010328
HD145906	16 15 46.3785238200	-49 15 12.234790296
HD326541	16 57 37.5608003112	-43 03 25.774942968
HD46107	06 31 36.3223323840	+04 55 59.555262108
HD93421	10 45 51.8197009104	-60 11 32.695283652
HD38023	05 42 21.3019719792	-08 08 00.178794456
HD95032	10 57 04.4851476360	-61 11 17.894992560
HD90786	10 27 25.2399582024	-59 56 43.394425188
HD303102	10 37 03.9908277648	-58 57 57.411324756
HD76220	08 55 23.9733707040	+19 41 59.548278696
HD90730	10 27 09.5323276824	-57 11 09.917651004
HD36938	05 34 56.2378081848	-04 45 57.382639308
HD177833	19 06 02.7612490800	+07 20 56.591874024
HD149780	16 38 59.7408131232	-45 35 35.804613696
HD150488	16 43 33.2566238376	-46 50 23.368388928
HD356242	19 55 01.095	+11 36 49.56
V* V351 Ori	05 44 18.7949456328	+00 08 40.410217104
HD231265	19 22 51.1252858680	+13 22 31.719515556
HD231244	19 22 10.6424279496	+14 00 58.256807760
HD34890	05 20 28.8919415400	-05 48 43.675848396
HD146726	16 20 10.5341163840	-51 14 13.440770088
HD231363	19 25 10.7241959712	+17 23 26.198377836
HD152593	16 56 08.5709343336	-42 36 12.077616816
HD147153	16 22 25.9901340720	-49 57 01.057836672
HD36444	05 31 40.4818564152	-01 07 33.281183208

**Table 6:** Sources, WISE slopes and disk contrast values.

Source	Right Ascension ( $^{\circ}$ $'$ $''$ )	Declination ( $^{\circ}$ $'$ $''$ )
HD36939	05 34 55.2955987536	-05 30 22.104460800
HD36998	05 35 13.2278636280	-04 35 40.989674688
HD146842	16 20 43.3009512744	-50 44 11.990240952
HD37114	05 35 58.5404909136	-05 22 31.373366988
HD149887	16 39 45.7770748800	-46 51 45.205408404
HD157189	17 23 13.7183387880	-31 29 25.871773740
HD34700	05 19 41.4089390784	+05 38 42.778590864
HD167499	18 16 13.6986042456	-16 48 06.397059492
HD167789	18 17 20.3236153392	-12 13 55.290477972
HD77400	09 00 25.4523398400	-47 15 22.429762956
HD142220	15 55 51.9243144000	-53 21 22.267354932
HD168279	18 19 42.7753245669	-18 09 45.575846973
HD146725	16 20 06.6273526200	-50 49 50.556038412
HD142675	15 58 19.0757522040	-53 00 00.146406348
HD154640	17 07 46.6134648192	-24 46 24.804478416
HD146522	16 19 08.3389865304	-51 05 38.564576016
HD37059	05 35 31.1580365376	-04 54 15.178126212
HD69710	08 16 18.4200229488	-44 20 36.554463024
HD98670	11 20 19.1934836760	-61 56 44.917578708
HD114670	13 13 16.5640747320	-63 18 00.812204172
HD319794	17 27 04.2360195168	-34 40 16.965180840
HD89725	10 19 40.1164681680	-58 05 46.898853936
HD106674	12 16 16.8233055528	-62 59 37.270725828
HD46388	06 33 20.3260006896	+04 38 58.042813308
HD98546	11 19 26.4642955416	-60 34 38.783965476
CD-25 4447	07 23 03.7629070872	-25 31 53.159850444
V* Z CMa	07 03 43.1599411656	-11 33 06.209065836
HD75347	08 47 55.7958690648	-42 35 22.195763484
HD37174	05 36 27.1856306736	-05 24 31.314914352
HD36983	05 35 07.6307079120	-05 52 08.399852760
HD147088	16 22 06.6928162584	-50 28 24.469189860
HD145703	16 14 48.4522821336	-51 48 31.411404072
HD95462	11 00 08.0378556624	-59 58 42.296754180
HD148140	16 28 22.8705281496	-48 19 14.041943544
HD316179	17 43 23.4355354704	-27 15 41.141282904
HD231276	19 23 12.0387	+13 20 18.487
HD93192	10 44 25.3545349128	-60 12 45.889745040
HD167086	18 14 25.0081355760	-17 57 10.664726436
HD149853	16 39 34.126	-46 39 01.33
HD58516	07 23 48.2389097280	-44 27 47.422412136
HD167475	18 16 06.2760419640	-17 05 07.697145120
BD-13 4924	18 18 34.4985881064	-13 54 21.986155800
HD148444	16 30 26.9933236224	-48 09 23.546417616
HD72087	08 29 30.8196998280	-38 36 55.882498536
HD124237	14 14 33.6804423288	-61 47 56.348540304
V* V970 Sco	17 39 41.2405860216	-32 17 57.527626920
HD143054	16 00 23.7394036104	-50 51 51.797018664
HD92909	10 42 19.3467768024	-59 10 15.462865668
HD95645	11 01 15.6171537504	-61 15 42.270959664
HD173724	18 46 50.6068551552	-02 22 37.661532996
HD339025	19 50 03.0950009280	+25 12 06.030906624
CD-51 9813	16 09 37.1578891152	-52 10 48.833629140
HD150040	16 40 42.68880	-47 40 07.7484
HD37060	05 35 34.2772048536	-05 06 21.214590156
HD166292	18 10 38.6868776856	-19 17 57.650427168

**Table 7:** Sources, WISE slopes and disk contrast values.

Source	Right Ascension ( $^{\circ}$ $'$ $''$ )	Declination ( $^{\circ}$ $'$ $''$ )
TYC 8696-83-1	15 43 00.2452458000	-54 00 27.523160604
HD231600	19 30 01.6554871920	+18 25 55.875046800
Gaia DR2 5942639	16 39 34.2015150895	-46 39 02.191084077
HD171837	18 37 14.6822375232	-06 36 17.823242124
HD94999	10 56 52.5439175808	-61 25 27.737164704
HD35336	05 23 34.1711611560	-11 58 40.656558972
HD294264	05 35 13.3447259856	-04 51 44.916838992
HD315052	18 03 49.8774768120	-25 04 44.344369380
HD318126	17 40 01.9611901536	-32 20 44.915290764
HD90979	10 28 50.8480250616	-56 44 15.086944356
HD162286	17 51 49.4776268568	-35 06 07.767522900
HD42575	06 11 19.1351435544	-05 11 28.237925328
HD116122	13 23 07.9830538464	-64 35 43.317306132
HD290812	05 40 57.4733795280	-01 50 15.330383772
HD46376	06 33 10.0730293392	+04 16 48.301680684
HD147071	16 22 00.6706260288	-50 19 34.209484536
HD149657	16 38 27.7671389400	-48 42 16.689627864
HD114719	13 13 39.5152822872	-63 41 01.459242312
HD326529	16 59 39.9264620904	-42 30 17.460950832
HD137997	15 31 52.4595136872	-56 10 40.698726744
HD166980	18 13 52.3558262640	-17 23 21.547553244
HD137924A	15 31 25.8928282650	-55 56 35.752275595
V* GW Ori	05 29 08.3928710640	+11 52 12.666457092
HD316314	17 46 39.0790054848	-28 53 51.715699008
HD15021	16 53 04.1811	-45 23 11.288
TYC 7880-485-1	16 54 09.4557844512	-43 11 41.355269304
BD+04 3964	19 04 20.8757670744	+05 06 56.200703904
HD127954	14 35 33.9462038952	-44 26 59.144520264
HD38040	05 42 40.4030802312	-04 49 11.971226460
HD77303	08 59 59.7339136200	-47 37 51.386592648
BD+04 3963	19 04 17.3166408144	+04 58 33.691665648
HD172617	18 41 19.9547868168	-03 47 02.885977752
HD145722	16 14 53.5930173120	-51 19 01.013897136
HD176013	18 58 05.1475160448	+01 36 18.745614360
HD298410	09 24 36.2104327032	-52 06 48.472715628
TYC 8697-1729-1	15 54 27.9917075832	-53 44 44.262213972
HD302527	10 10 13.3440783312	-57 18 21.908124864
HD167898	18 17 39.1815723120	-09 22 04.179001980
HD126359	14 27 44.2402112904	-65 08 36.276684216
CPD-24 6153	18 04 12.7770066528	-24 21 42.885958896
HD231231	19 21 45.8871210168	+14 21 50.190116112
HD303181	10 39 05.7587965728	-58 46 04.966146048
HD319788	17 26 26.4630612072	-34 17 01.043880360
HD8735	01 25 14.6406976368	-45 56 28.179942360
HD146258	16 17 48.3211163112	-50 58 05.168519868
HD155893	17 16 07.3275600216	-38 51 18.015593616
HD79964	09 15 24.4079958768	-47 44 18.397640724
HD179262	19 11 31.2293018376	+10 25 02.845553556
HD178827	19 09 44.4426	+08 32 22.129
TYC 8696-627-1	15 40 00.1193369760	-54 00 14.075790984
CD-70 776	11 02 04.4192916024	-71 29 53.692033308
HD94172	10 50 54.7461555432	-59 51 12.366696924
HD174752	18 52 09.3151271328	-00 57 38.666229768
HD156588	17 20 06.7696849800	-37 15 26.997527952
HD167770	18 17 33.2168455080	-17 56 52.628795088
HD174130	18 49 02.3218873290	-00 50 30.739894654

**Table 8:** Sources, WISE slopes and disk contrast values.

Source	Right Ascension ( $^{\circ}$ ' '')	Declination ( $^{\circ}$ ' '')
HD77538	09 01 22.1631861912	-48 53 48.559259112
HD158199	17 29 30.3345364824	-35 41 30.615006048
HD165088	18 06 28.0320331872	-44 54 54.327866652
HD37489	05 39 22.3318651752	+08 12 29.957520420
CD-61 4191	14 03 56.1788307888	-62 19 55.130205468
HD173725	18 46 58.9696631304	-03 46 48.124285824
HD87542	10 03 53.7900934656	-57 46 34.286508516
HD161274	17 45 51.3378610992	-29 30 46.513185768
HD95732	11 01 48.9265931064	-61 46 27.129507600
CI Trumpler 16 35	10 44 29.8551483960	-59 32 18.420466380
HD154071	17 05 10.1166025848	-40 42 07.666898220
HD173990	18 48 45.4836790584	-11 42 18.811177308
HD93402	10 45 47.0995938240	-58 40 47.370033264
CD-38 4128	08 09 28.6435040016	-38 51 29.283725484
* zet Ori C	05 40 46.1671174152	-01 55 36.349356360
HD171429	18 35 10.4020334856	-07 24 52.962917292
HD36937	05 35 00.1416426096	-04 31 36.556924332
HD164882	18 04 14.9237465160	-22 03 32.119398468
HD147012	16 20 19.3660079880	-25 36 43.055007840
HD318084	17 41 47.1076189704	-32 05 34.474355016
HD258592	06 30 14.9654176464	+04 26 36.497655852
HD156100	17 17 08.1003499032	-34 07 10.289791452
HD36899	05 34 42.2804860032	-05 07 14.579496804
HD151160	16 47 48.1475352960	-46 15 00.510206868
HD322601	17 00 25.0375958688	-40 30 24.763357260
HD158124	17 28 52.8779560632	-34 45 37.180796472
HD159214	17 34 59.1134721024	-33 36 53.496012060
BD-06 4822	18 38 36.2583592800	-05 57 03.397797540
HD319798	17 27 53.7206431176	-34 57 42.873309576
HD145907	16 15 42.3152814192	-50 05 04.169718204
CD-40 4131	08 21 19.7706519600	-40 37 21.703389744
HD60842	07 29 31.9735797120	-73 22 43.335802128
TYC 9006-4324-1	14 26 55.3006866960	-60 45 53.099678628
HD151729	16 51 15.9750629688	-45 41 40.730056944
HD98421	11 18 31.8504459024	-60 49 16.662750456
HD179150	19 11 06.2479713312	+09 38 44.093907924
HD294262	05 35 18.4437121896	-04 40 55.861089528
HD322486	17 01 19.3836403776	-38 10 57.247283028
HD35733	05 26 42.1362277008	-04 11 31.862109984
HD170634	18 30 24.8757877680	+01 13 23.641855860
BD-12 5011	18 20 35.8028772984	-12 50 52.787897268
HD168447	18 20 23.1205288128	-15 56 25.310272128
HD35978	05 22 59.8006192008	-68 03 51.209963208
HD245168	05 35 02.9980210752	+09 56 04.798296348
V* MX Ori	05 35 21.2653329384	-05 09 16.174506564
HD306088	11 07 35.9119554192	-60 36 48.081502620
BD-13 4917	18 18 06.4005383520	-13 36 26.395722216
HD179839	19 13 42.2683979448	+10 58 59.759947668
HD326758	17 06 48.8393099208	-41 01 13.992928284
HD148446	16 30 26.9986170024	-48 44 19.503276648
HD295044	06 25 07.9134764265	-04 51 29.899356571
HD198147	20 53 24.0848529864	-71 50 13.904576124
HD161647	17 47 56.6712282504	-29 32 59.641484244
HD153327	16 59 51.8000627592	-25 10 18.805370700

**Table 9:** Sources, WISE slopes and disk contrast values.

Source	Right Ascension ( $^{\circ}$ , $''$ )	Declination ( $^{\circ}$ , $''$ )
HD287823	05 24 08.0485208544	+02 27 46.884084984
HD160747	17 42 54.1858623288	-29 58 42.215347020
HD161526	17 47 11.6102003544	-28 42 47.890803600
TYC 8613-376-1	10 37 17.2382421648	-58 42 33.050352600
HD92086	10 36 34.9978949448	-58 50 16.429124256
HD346346	20 21 11.5920779160	+24 33 12.582502740
TYC 5689-715-1	18 21 03.6751466808	-14 09 42.083987508
HD290815	05 40 56.7248134416	-02 08 57.180136848
HD290599	05 32 50.4235907880	-01 36 02.748252348
BD+03 3860	18 59 47.3067056496	+04 06 45.071283816
HD172788	18 42 15.2216775168	-02 19 42.634257528
BD-20 1321	06 12 04.1843198568	-20 54 39.069330264
HD156527	17 19 47.0782293672	-39 17 41.338118436
HD149207	16 35 33.7194626688	-48 56 01.941962784
HD303314	10 42 39.1122229176	-59 28 16.382047080
HD174025	18 48 36.8729479272	-01 10 34.694336280
BD-05 1322	05 35 26.1704698248	-05 48 16.634635488
HD36105	05 29 24.8431616478	+03 43 30.533661357
TYC 8702-1182-1	15 13 47.6558924232	-56 25 43.909973436
IRAS 05509+0921	05 53 42.5215927944	+09 21 45.383643504
HD314896	18 01 31.4735545416	-24 08 10.339277604
HD317804	17 34 10.8866627712	-31 42 59.120093844
CD-58 5802	14 49 18.8739310872	-59 24 47.845963836
V* V971 Sco	17 40 12.6408982440	-32 09 32.843045556
HD122417	14 03 48.5717129952	-61 56 40.473443400
HD78580	09 07 20.7394904976	-47 06 55.098559548
V* V1247 Ori	05 38 05.2519466880	-01 15 21.698856468
HD290674	05 36 57.3189250970	-01 26 07.424856469
HD313634	18 01 00.2027840664	-23 54 36.422201880
HD125670	14 23 07.2233531520	-60 25 47.913582756
HD310494	11 20 02.3289312048	-65 15 59.564589264
CD-48 11055	16 40 43.6046996544	-48 48 51.871502340
HD344791	19 43 20.2836723912	+23 01 45.595345872
HD290469	05 27 38.6135339688	-01 58 01.835209344
HD150794	16 45 16.2530964456	-45 00 20.882695968
HD262014	06 41 15.3017068824	+09 31 16.324176252
HD338985	19 50 25.6365131256	+26 27 14.488759116
BD-12 5050	18 27 02.0861409024	-12 50 19.793139684
HD312742	18 12 33.7226708136	-18 28 56.276573988
HD284346	04 19 46.1848130208	+19 45 39.849619680
HD312744	18 12 28.6214475384	-18 38 51.037190916
HD108983	12 31 49.9853735784	-62 14 05.541609516
HD59049	07 27 26.5682095902	-20 07 57.788019480
HD167547	18 16 27.3604351248	-17 34 26.351132700
CD-43 4652	08 47 54.1560569304	-43 34 01.683448644
CD-42 4817	08 57 34.1453656392	-42 43 56.200845468
HD68695	08 11 44.5714665288	-44 05 08.777141772
HD77652	09 02 09.0177986400	-46 55 53.711084388
HD89045	10 14 45.8213629584	-57 52 31.923079392
HD168077	18 18 34.2654608184	-14 13 24.094393572
HD106415	12 14 35.5453791888	-51 33 07.506057996
HD95020	10 56 57.7727195856	-61 06 38.674092600
HD164189	18 00 47.8507736280	-18 45 17.402482044
HD92251	10 37 43.6425305952	-59 29 48.459453540
HD258690	06 30 40.2518397600	+05 22 38.775780588

**Table 10:** Sources, WISE slopes and disk contrast values.

Source	Right Ascension (°, '')	Declination (°, '')
HD146184	16 17 23.7501977304	-50 51 53.649709092
HD339094	19 51 54.6181037736	+26 29 09.862485360
HD231581	19 29 34.31424	+17 59 46.0284
HD129644	14 46 01.1761569384	-59 16 05.108053332
2MASS J08161-3449	08 16 15.3117152880	-34 49 37.072542792
CD-32 13089	17 40 02.9974568976	-32 13 19.684298172
HD99192	11 24 06.9464132400	-61 43 43.145366232
HD143816	16 05 07.2813714552	-53 14 43.532406384
HD125832	14 24 19.9150785672	-62 10 58.069479756
HD56192	07 13 47.7660095880	-46 34 58.726576632
HD318099	17 40 17.7970966296	-32 10 58.322790048
HD295181	06 33 37.7652176112	-04 50 55.719992724
CPD-57 4258	11 06 08.3682363864	-58 40 14.660087196
HD326596	16 58 07.7540138640	-44 00 13.497349968
TYC 453-327-1	18 56 09.5638891248	+02 17 43.770440436
HD317975	17 37 03.2599680288	-32 33 43.562608992
HD302670	10 19 15.9961855536	-58 06 45.376388352
CD-38 4381	08 23 11.8586968392	-39 07 01.621267032
CD-41 11284	17 08 07.3413302208	-41 39 27.563132268
HD305519	10 44 11.2479486792	-59 55 30.689679936
V* V1366 Ori	05 16 00.4765181328	-09 48 35.393784012
HD139948	15 43 32.7260715768	-54 03 20.578783716
HD174374	18 50 20.7972560568	-01 35 08.807405532
IRAS 05291+1058	05 31 52.9046439525	+11 00 38.154706774
TYC 8608-774-1	10 14 29.1255019272	-57 37 51.419943696
TYC 8994-1530-1	13 11 59.4362483664	-63 14 23.095957308
TYC 457-421-1	18 56 57.0985448856	+04 07 18.020033904
HD132608	15 02 51.8103461856	-61 48 44.287719588
HD150356	16 42 46.5555368208	-46 11 56.692605660
BD-05 4711	18 38 38.4686568672	-05 50 05.062647084
HD146801	16 20 29.2379724120	-50 35 16.061866332
BD-11 4595	18 19 47.2412214216	-11 54 52.972983864
HD306170	11 14 33.4939008744	-60 45 32.839219656
HD323017	17 18 04.0352893560	-38 22 52.002234912
HD37130	05 36 03.5675776920	-04 45 07.631549964
HD156807	17 21 26.4945534192	-38 43 02.327995956
HD168182	18 18 56.7103762416	-11 17 00.026163960
HD161757	17 48 37.5495786768	-29 28 27.977876508
BD+00 2004	07 35 35.8414628280	+00 14 15.505524600
HD148471	16 30 31.1441689296	-47 10 24.454222140
HD166077	18 09 43.7551521168	-19 18 51.642648360
HD156783	17 21 13.8791619504	-37 18 56.713163544
BD+01 3810	18 54 05.2494	+01 12 07.325
HD328991	16 50 30.6862244904	-46 10 03.358316172
HD147358	16 23 50.2324652064	-49 23 54.125560680
HD178164	19 07 16.3498030848	+07 04 52.944323916
BD-06 4814	18 37 29.7877023072	-06 10 34.441018356
CD-32 12630B	17 20 26.8033135848	-33 05 08.652248304
HD327114	17 15 35.5984529976	-41 21 05.749158348
HD329102	16 53 55.8904719696	-45 16 38.412987420
HD155476	17 13 33.4344584424	-39 00 37.041201288
HD284470A	04 28 06.4772917248	+19 36 06.678334152
HD86835	09 59 28.6787803584	-56 56 16.089608400
BD-02 4739	18 46 50.6922215760	-02 29 07.300103352
TYC 7872-1109-1	16 55 00.2902679328	-39 42 03.734786376
HD69189	08 14 05.5059434712	-41 40 04.488117816

**Table 11:** Sources, WISE slopes and disk contrast values.

Source	Right Ascension (°, '')	Declination (°, '')
HD178931	19 11 16.0987092696	-20 48 19.106317836
TYC 9006-71-1	14 22 33.6838621080	-61 08 56.375814372
HD317957	17 37 06.7494688104	-31 58 35.711594580
HD315011	18 03 29.8927298520	-24 01 07.789580796
HD298349	09 19 12.1723045848	-52 01 12.990154728
TYC 1397-1374-1	08 54 18.6074409168	+19 54 28.624031856
HD303166	10 39 19.6390988880	-58 16 00.279711588
HD147087	16 22 01.7707311120	-48 41 05.422374276
HD121364	13 56 53.5865760744	-61 36 24.477666552
HD174241	18 49 40.9297454592	-00 49 54.292075068
HD139617	15 41 32.7290558184	-53 57 47.790869328
BD-05 1296	05 33 55.2338099208	-05 38 50.561757888
HD178641	19 09 27.9545543760	-00 49 45.122322324
HD316300	17 47 54.1792833216	-28 37 35.975867052
HD231557	19 29 06.6615681936	+16 46 12.906734412
HD149399	16 36 44.1023303952	-48 04 29.020256184
HD82666	09 31 36.7882470072	-52 29 15.799251660
HD84150	09 41 19.0475266920	-54 14 35.602300860
HD145684	16 14 35.0076956184	-49 48 13.970328984
HD111150	12 47 54.5670890568	-63 27 05.606710524
HD181311	19 20 19.2492726600	-08 03 41.987268900
HD312682	18 09 12.0205440864	-20 15 10.031683572
HD148012	16 27 36.1046515128	-49 49 18.326846244
TYC 8978-4360-1	12 10 58.4536724208	-62 39 25.481079000
BD-17 5780	19 52 53.4532	-16 59 56.055
HD328756	16 45 01.6103438784	-45 14 38.886324936
HD319732	17 23 07.4296560864	-35 58 46.892044236
HD293815	05 06 51.0557695968	-03 19 59.949324624
HD352873	20 44 01.8567334800	+19 12 46.352924172
TYC 470-1071-1	19 01 48.1237570296	+04 13 04.929065076
HD259107	06 31 55.2084134400	+04 14 27.274045596
HD450	00 08 58.4105534376	-00 15 23.127384492
HD166981	18 13 52.8685060512	-17 54 40.211730144
BD+05 4033	19 06 55.7279893104	+05 14 33.701003700
HD167111	18 14 37.2003089472	-17 54 26.685141012
HD323397	17 25 54.3056418576	-40 14 41.139150648
TYC 8957-1247-1	10 47 07.7961131472	-60 09 30.225834396
BD-05 1299	05 34 14.1619196472	-05 36 54.187822224
CD-29 10315	13 24 29.1359054832	-30 26 02.108736132
HD287841	05 24 42.8032369656	+01 43 48.249234516
TYC 139-1242-1	06 12 19.2101353824	+04 31 36.583589244
HD231654	19 31 10.3600022976	+18 31 38.688931848
TYC 5113-730-1	18 43 49.1658157392	-01 51 17.353161468
CD-53 6343	15 59 34.4371415592	-53 43 32.122482240
HD71078	08 23 41.1817010592	-42 49 54.969403764
TYC 470-986-1	19 00 48.6888511464	+03 57 45.388106280
HD302960	10 31 47.0018076144	-58 03 44.814316392
HD156918	17 21 55.5730837656	-38 16 28.312145940
HD315193	18 07 02.2632866880	-25 36 57.713901696
CD-42 4710	08 50 47.4001881456	-43 02 18.821016420
HD330981	16 38 49.1516237568	-47 40 11.935308972
HD302577	10 12 35.9110622856	-57 35 48.250033620
BD+00 4053	18 55 32.3496588024	+00 48 29.148948180
HD287802	05 22 52.9370554632	+00 55 57.864144576
HD322677	17 04 07.7247960144	-38 15 40.002220584
HD326414	16 55 13.5026676048	-43 07 00.293770200

**Table 12:** Sources, WISE slopes and disk contrast values.

Source	Right Ascension ( $^{\circ}$ $'$ $''$ )	Declination ( $^{\circ}$ $'$ $''$ )
HD282276	04 33 04.2302284416	+29 21 49.832827884
TYC 474-440-1	19 04 24.6252	+05 43 16.593
HD147826	16 26 29.2071334224	-48 49 15.147972696
HD159805	17 38 02.6232812568	-31 50 50.521152552
HD318309	17 48 20.4645188568	-31 23 13.699925376
TYC 7366-1340-1	17 20 47.5520251608	-33 42 18.075764808
HD171956	18 37 48.5099867184	-08 44 30.502256496
HD67129	08 04 28.7871291792	-48 15 47.717555652
TYC 9007-5578-1	14 40 42.2325347856	-60 49 10.024518288
TYC 7870-1041-1	17 17 23.2520618712	-38 51 25.167857184
BD-05 1307	05 34 52.2399438744	-05 33 08.495625096
HD322436	16 57 40.7738629440	-40 31 46.542554292
HD109102	12 32 40.2978941400	-62 43 14.649360996
HD312769	18 09 32.5677762816	-19 03 15.578023428
HD153308	17 00 30.3256998336	-40 18 16.494911136
TYC 6265-2443-1	18 17 36.5660651088	-16 43 57.673936776
HD305886	11 02 27.1578417288	-60 45 06.416185248
CD-42 4753	08 53 04.7839596720	-42 34 31.502706240
CD-51 9983	16 18 24.7687740528	-51 39 08.665683444
HD157385	17 24 29.8554042024	-36 44 51.857280384
TYC 8697-1600-1	15 53 47.9225200224	-53 22 27.403484304
CD-61 3679	13 09 27.7018351920	-62 13 05.960161740
HD317867	17 32 44.3121162024	-32 57 53.992287144
TYC 8702-912-1	15 18 53.1197346936	-56 44 00.590501184
HD259013	06 31 36.0860760144	+04 47 45.610662084
BD+22 3788	19 43 41.9250883368	+23 16 10.561470384
CPD-62 2609	12 10 54.3390053256	-62 57 21.924545796
TYC 5685-2511-1	18 17 28.4126405448	-12 32 04.705040364
HD171390	18 34 53.3131127616	-08 37 55.660360836
CPD-53 6816	15 56 40.3841317296	-54 21 53.105767776
TYC 272-777-1	11 49 48.6848466480	+01 34 37.802932896
HD338935	19 47 20.6356359696	+24 37 11.073262368
HD231695	19 31 51.6305623032	+18 38 44.490518700
TYC 9005-673-1	14 16 33.2051670384	-61 38 43.801180620
BD+01 3817	18 54 55.7507804976	+01 15 13.921440732
CD-41 4599	08 52 18.4483757760	-42 11 52.292074272
TYC 8942-2872-1	09 54 50.3102395656	-60 35 54.892694688
TYC 8696-931-1	15 42 20.9453265240	-54 20 42.259020252
HD117258	13 30 38.3587264488	-62 59 55.360508208
V* V1321 Ori	05 35 04.3009445808	-05 08 12.737523192
HD317948	17 37 28.4172352128	-31 49 38.034984360
CD-52 7168	16 01 28.1116864392	-52 23 57.937168248
TYC 2137-1321-1	19 30 44.2742065320	+29 28 04.496330496
CD-49 11075	16 57 22.3309243728	-49 48 36.779815188
HD339533	20 07 24.7058540928	+27 33 03.932300520
TYC 1322-515-1	06 08 35.1023445000	+20 26 29.083365960
TYC 8703-1220-1	15 24 59.0630315928	-56 20 45.822827040
CD-42 4623	08 47 20.5687489032	-42 43 27.807774816
HD205805	21 39 10.6154323536	-46 05 51.525534876
HD328940	16 47 46.8687758328	-45 08 44.171304180
HD290603	05 33 38.2226718312	-01 35 26.935233756
BD-05 1297	05 34 11.1261387072	-05 22 54.597327420
HD319901	17 28 26.9123206848	-35 07 00.811927416

**Table 13:** Sources, WISE slopes and disk contrast values.

Source	Right Ascension ( $^{\circ}$ , $''$ )	Declination ( $^{\circ}$ , $''$ )
HD171093	18 33 00.942	-05 16 16.57
CD-51 9790	16 07 22.7628694608	-51 23 44.001620448
HD302598	10 11 30.8244865728	-58 57 48.635109936
HD170059	18 28 04.5192147432	-13 44 10.251837456
HD302531	10 08 21.5777300520	-57 21 05.724013248
HD315847	17 26 58.1314641072	-30 06 21.661311420
HD38563	05 46 44.658	+00 05 22.78
HD135042	15 15 41.5122950352	-58 07 44.151808692
HD318102	17 39 42.4234860456	-32 05 57.251354964
HD259512	06 33 08.7339897888	+04 45 47.080680624
TYC 1948-685-1	08 38 20.1983450232	+28 38 23.091389916
TYC 9005-144-1	14 15 46.0399414488	-60 03 41.930956332
HD290862	05 46 43.3856873232	+00 04 36.042148164
HD259835	06 34 06.9825481128	+04 47 26.082228156
TYC 1300-2029-1	05 27 46.7388370224	+17 44 07.534541976
BD-13 4945	18 20 42.9313009728	-13 33 40.997898936
HD121918	14 00 27.3419605992	-62 46 39.866388060
BD-06 4632	17 42 38.6014083576	-06 27 04.057470108
CD-43 7823	12 42 10.6696492296	-43 56 39.869671848
BD-04 4539	18 40 00.9366350736	-04 50 26.519653176
HD298366	09 15 20.3879547216	-52 45 21.906257688
HD138828	15 37 19.2979014672	-56 47 36.835112364
HD229556	18 48 20.2800632568	+19 06 32.481804780
BD-04 4566	18 44 24.7420087968	-04 19 00.368717160
BD-06 1256	05 36 37.8106367904	-06 25 30.135833220
CD-27 2802	06 12 32.0914644288	-27 11 10.879140984
HD126907	14 30 50.9352986064	-62 09 36.834774120
NGC 2244 278	06 32 33.2041388832	+04 44 53.320251264
HD335743	18 12 58.1935319256	+27 28 01.372052928
HD167373	18 15 37.5657278424	-17 05 52.571008932
TYC 8979-134-1	12 18 04.3031832504	-62 24 34.273702620
HD156722	17 20 43.0758678120	-33 08 40.103630196
TYC 8626-905-1	10 41 09.6278487480	-59 23 46.514003748
HD261389	06 39 15.8034521784	+08 46 00.504839028
TYC 8697-1608-1	15 58 00.8079327216	-53 37 32.987823060
CD-32 13093	17 40 06.8713463040	-32 13 50.699474652
BD-20 4696	17 16 06.4946169432	-21 01 58.313537652
TYC 9006-3698-1	14 22 46.0151061432	-61 02 30.633784440
HD259014	06 31 38.3150382240	+04 20 28.094868168
HD328672	16 42 45.4460971608	-46 34 41.145697128
HD328654	16 41 09.1681731672	-46 04 49.186794000
HD322456	16 56 48.3551083392	-40 49 06.806952732
HD90101	10 22 37.2919874808	-57 27 13.411099332
CD-43 4664	08 48 33.4078250256	-43 30 17.458677216
HD330567	16 19 41.9678568432	-50 10 31.870943760
HD317857	17 34 34.1882020848	-32 36 08.936209656
TYC 105-2475-1	05 28 59.7066468696	+03 21 48.628187856